Journal of Power Sources 186 (2009) 353–369

Contents lists available at ScienceDirect

Journal of Power Sources

journal homepage: www.elsevier.com/locate/jpowsour

Review

Microfluidic fuel cells: A review

Erik Kjeang[a,b,*], Ned Djilali[a,b], David Sinton[a,b]

[a] Department of Mechanical Engineering, University of Victoria, 3800 Finnerty Road, Victoria, BC, Canada V8W2Y2
[b] Institute for Integrated Energy Systems (IESVic), University of Victoria, 3800 Finnerty Road, Victoria, BC, Canada V8W2Y2

ARTICLE INFO

Article history:
Received 15 August 2008
Received in revised form 2 October 2008
Accepted 2 October 2008
Available online 17 October 2008

Keywords:
Fuel cell
Biofuel cell
Microfluidic
Membraneless
Laminar flow
Review

ABSTRACT

A microfluidic fuel cell is defined as a fuel cell with fluid delivery and removal, reaction sites and electrode structures all confined to a microfluidic channel. Microfluidic fuel cells typically operate in a co-laminar flow configuration without a physical barrier, such as a membrane, to separate the anode and the cathode. This review article summarizes the development of microfluidic fuel cell technology, from the invention in 2002 until present, with emphasis on theory, fabrication, unit cell development, performance achievements, design considerations, and scale-up options. The main challenges associated with the current status of the technology are provided along with suggested directions for further research and development. Moreover, microfluidic fuel cell architectures show great potential for integration with biofuel cell technology. This review therefore includes microfluidic biofuel cell developments to date and presents opportunities for future work in this multi-disciplinary field.

Contents

* Corresponding author. Present address: Ballard Power Systems, Inc., 9000 Glenlyon Parkway, Burnaby, BC, Canada V5J5J8. Tel.: +1 604 415 7248; fax: +1 604 412 4700.
E-mail address: ekjeang@gmail.com (E. Kjeang).

0378-7753/$ – see front matter © 2008 Elsevier B.V. All rights reserved.
doi:10.1016/j.jpowsour.2008.10.011

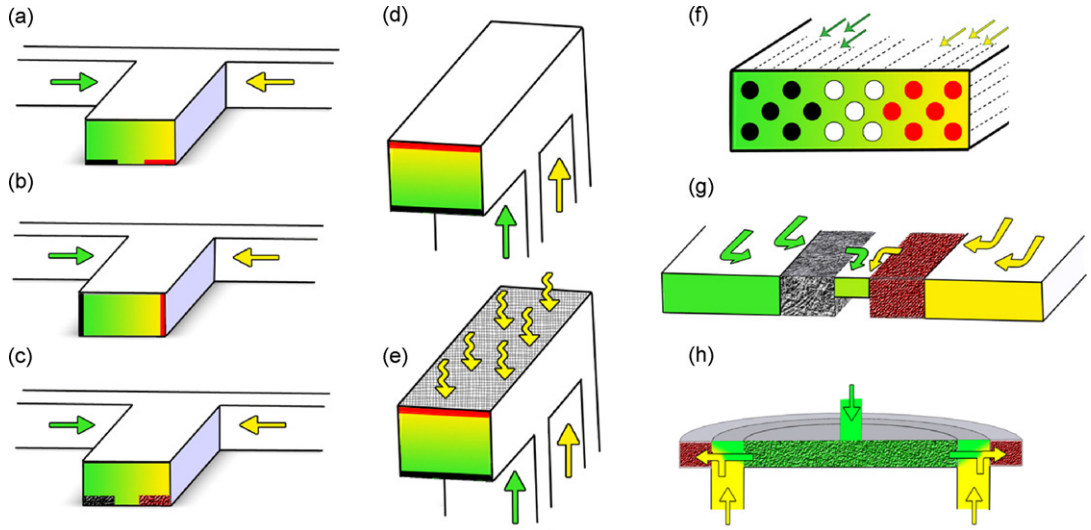

Fig. 1. Schematic of co-laminar microfluidic fuel cell architectures. Laminar streaming, characteristic of microfluidic liquid flows, facilitates the separation of fuel and oxidant in the absence of a membrane. Each architecture is shown with fuel in green, oxidant in yellow, cathodes in red, anodes in black, and porous electrodes textured. Two streams are combined horizontally in a T- or Y-channel with electrodes on bottom (a), electrodes on sides (b), and porous electrodes on bottom (c). An F-channel configuration (d), and with the addition of a porous electrode to facilitate air-breathing (e). An electrode array microfluidic fuel cell (f). A flow through porous electrode microfluidic fuel cell (g). A radial porous electrode fuel cell architecture (h).

1. Introduction

Many different types of fuel cells are currently under development, with a variety of targeted applications ranging from miniature power supplies to large-scale combined heat and power plants [1]. With the exception of limited small-scale commercialization of some stationary units, most of these fuel cells have not yet gone beyond the field trials stage. Small fuel cells for portable electronic equipment are considered rather close-to-market for a number of reasons [2]: it is unlikely that the technical development of batteries will keep pace with the accelerating power demands; small, microstructured fuel cells enable higher overall energy density than batteries; and the market for portable electronics has an inherently high cost tolerance. Small fuel cell technologies employing conventional electrocatalysts have been dominated by hydrogen-based proton exchange membrane (PEM) fuel cells and direct liquid fuel cells [3–6], as well as mixed-reactant fuel cells with selective catalysts [7]. Miniaturized fuel cell devices employing biological catalysts have also been demonstrated, collectively termed biofuel cells [8,9], including microbial fuel cells [10,11] and enzymatic biofuel cells [12,13]. There are still some technical challenges, though, related to the development of miniaturized fuel cell technologies. Hydrogen-based fuel cells require hydrogen storage units that are generally too bulky for portable device applications, and direct liquid fuel cells, with compact fuel storage solutions, suffer from reduced cell voltage due to slow electrochemical kinetics and fuel crossover from anode to cathode. Biofuel cell technologies have shown relatively low power densities and limited stability associated with the lifetime of the biological components.

Micro and nanofluidic devices for energy conversion were recently reviewed by Pennathur et al. [14], with emphasis on miniaturization of conventional energy conversion machines and nanofluidic streaming potential devices. Microfluidic fuel cells, sometimes called laminar flow-based fuel cells or membraneless fuel cells, describes a group of fuel cells capable of operation within the framework of a microfluidic chip. A microfluidic fuel cell is defined as a fuel cell with fluid delivery and removal, reaction sites and electrode structures all confined to a microfluidic channel. This type of fuel cell operates without a physical barrier, such as a membrane, to separate the anode and the cathode, and can use both metallic and biological catalysts.

Fig. 1 shows schematically various microfluidic fuel cell architectures presented to date. These architectures include the common configurations where two streams are combined horizontally in a T- or Y-channel with: electrodes on bottom (Fig. 1a); electrodes on sides (Fig. 1b); and porous electrodes on bottom (Fig. 1c). Using an F-channel configuration, streams are combined vertically via sheath-flow with electrodes on top and bottom (Fig. 1d). The F-channel configuration also permits the use of a porous electrode on top, as in the air-breathing architecture (Fig. 1e). The electrode array microfluidic fuel cell employs microfluidic flow between solid, free standing electrodes in a hexagonal pattern (Fig. 1f). In the flow through porous electrode microfluidic fuel cell (Fig. 1g), reactants flow through and react within porous electrodes prior to combining in a co-laminar waste stream. The radial porous electrode fuel cell architecture utilizes sequential flow of fuel and oxidant in a concentric fashion (Fig. 1h).

In the most common configurations, microfluidic fuel cells utilize the laminar flow characteristic of microfluidic flows to delay convective mixing of fuel and oxidant. This flow regime is characterized by low Reynolds' numbers, $Re = \rho U D_h/\mu$, where ρ is the fluid density, U is the average velocity, D_h is the hydraulic diameter, and μ is the dynamic viscosity. At low Reynolds' number, two aqueous streams, one containing the fuel (anolyte) and one containing the oxidant (catholyte), will flow side-by-side down a single microfluidic channel, as shown in Fig. 1a. The anolyte and catholyte also contain supporting electrolyte that facilitates ionic transport within the streams, thereby eliminating the need for a separate electrolyte. Mixing of the two streams occurs by diffusion only, and is restricted to an interfacial width at the center of the channel. The mixing width can be controlled by modification of channel dimensions and flow rate, and the electrodes are integrated on the walls of the manifold with sufficient separation from the co-laminar inter-diffusion zone in order to prevent fuel crossover.

The microfluidic fuel cell design avoids many of the issues encountered in PEM-based fuel cells, for example humidification, membrane degradation, and fuel crossover. The co-laminar configuration also allows the composition of the anolyte and catholyte

streams to be chosen independently, thus providing an opportunity to improve reaction rates and cell voltage. In addition to compactness, miniaturization of fuel cells has a further advantage: a high surface-to-volume ratio, which scales as the inverse of the characteristic length. Since electrochemical reactions are surface-based, the performance of the fuel cell benefits directly from miniaturization of the device. The most prominent benefit related to microfluidic fuel cells, however, is the economical aspect. Microfluidic fuel cells can be manufactured by inexpensive, well-established micromachining and microfabrication methods and the cost associated with the membrane, which is significant for most other fuel cells, is eliminated. In addition, microfluidic fuel cells are normally operated at room temperature and require no auxiliary humidification, water management, or cooling systems. Before it is possible to capitalize on the advantages of microfluidic fuel cells, however, significant progress is required in terms of energy density and fuel utilization.

This review article summarizes the development of microfluidic fuel cell technology to date and provides an overview of the challenges that need to be overcome to reach commercial applications. The operational principles of a microfluidic fuel cell based on co-laminar flow are described, and the performance and viability of current microfluidic fuel cell devices are compared, with consideration of choice of reactants, electrochemical reactions, transport characteristics and cell architectures. Finally, the potential benefits of combining biofuel cell technology with state-of-the-art microfluidic fuel cell designs are discussed.

2. Fundamentals

Microfluidics [15,16] is defined as the science of fluid flow and transport phenomena in microstructures with at least one characteristic dimension in the range of 1–1000 μm. This multidisciplinary field lies at the interface of engineering, chemistry and biology and has a wide range of applications including drug discovery, biomedical analyses, genetics, proteomics, and energy conversion. Squires and Quake [17] and Gad-El-Hak [18] provide useful reviews of the fluid physics of microfluidic networks, and an overview of numerical modeling of microfluidic transport phenomena is available by Erickson [19]. Fluid flow in microscale devices is typically laminar and governed by low Reynolds numbers, where viscous effects dominate over inertial effects and surface forces are more relevant than body forces. Due to the laminar nature of microfluidics, the velocity field $\bar{u}$ for incompressible Newtonian fluids can be deduced by solving the Navier–Stokes equations for momentum conservation in 3D, provided that the continuum assumption is appropriate (as in most microscale liquid flows) [16–18]:

$$\rho\left(\frac{\partial \bar{u}}{\partial t} + \bar{u}\cdot\nabla\bar{u}\right) = -\nabla p + \mu\nabla^2\bar{u} + \bar{f} \tag{1}$$

Here, p represents pressure and $\bar{f}$ summarizes the body forces per unit volume. At very low Reynolds numbers, the non-linear convective terms can be neglected, resulting in linear and predictable Stokes flow:

$$\rho\frac{\partial \bar{u}}{\partial t} = -\nabla p + \mu\nabla^2\bar{u} + \bar{f} \tag{2}$$

Furthermore, mass conservation for fluid flow obeys the continuity equation:

$$\frac{\partial \rho}{\partial t} + \nabla\cdot(\rho\bar{u}) = 0 \tag{3}$$

For a fluid with constant density this leads to the incompressibility condition $\nabla\cdot\bar{u} = 0$. A parabolic velocity profile is obtained for pressure driven flow, whereas the velocity profile for electroosmotic flows is flat and uniform across the channel.

Another important feature of the microscale is that the surface area to volume ratio, which is inversely proportional to the characteristic length, is very high in these devices. A high surface to volume ratio promotes heterogeneous chemical reactions such as the electrochemical reactions occurring in fuel cells. In principle, the smaller one can make the characteristic size of the microchannel, the better, since the fuel cell device would generate more power in the same volume. Reducing the size of the channel will however increase the parasitic load required to drive the flow, and ultimately the net power generation would diminish. The pressure drop for pressure-driven laminar flow with mean velocity U in a channel of length L and hydraulic diameter D_h is given by [20]:

$$\nabla p = \frac{32\mu LU}{D_h^2} \tag{4}$$

Further, the pumping power W is obtained by multiplying the pressure drop by the flow rate Q:

$$W = \nabla pQ = \frac{32\mu LUQ}{D_h^2} \tag{5}$$

Note that the pumping power calculated from Eq. (5) provides an estimate based on fully developed flow in a straight channel, neglecting the contributions from inlet and outlet feed sections and other minor losses.

Controlled microfluidic fluid–fluid interfaces [21] provide unique functionality. For example, when two laminar streams of similar fluids in terms of viscosity and density are brought into a single microfluidic channel, a parallel co-laminar flow is developed with a fluid–fluid interface that has useful properties for many applications. Species transport within microscale flows normally takes place under the effects of convection/diffusion, electromigration, and chemical reaction. In the absence of chemical reaction and electromigration, mixing between two co-laminar streams occurs by transverse diffusion alone. Microscale devices generally experience high Péclet numbers, $\mathrm{Pe} = UD_h/D$, i.e. the rate of transverse diffusion is much lower than the streamwise convective velocity, and the diffusive mixing is therefore restricted to a thin interfacial width in the center of the channel that grows as a function of downstream position (z) and mean velocity. The inter-diffusion zone has an hourglass shape with maximum width (δ_x) at the channel walls according to the following scaling law [22] for pressure-driven laminar flow of two aqueous solutions:

$$\delta_x \propto \left(\frac{DHz}{U}\right)^{1/3} \tag{6}$$

Here, D represents the diffusion coefficient and H is the channel height. The inter-diffusive scaling law given in Eq. (6) is however limited to liquids of similar density. When two liquids of different densities are employed, a gravity-induced reorientation of the co-laminar liquid–liquid interface occurs, which was analyzed quantitatively by Yoon et al. [23]. The physics of co-laminar flow is the core mechanism in several microfluidic devices such as the T-sensor [24], Y-mixer [25], and H-filters [26]. A T-sensor, for example, can be employed to measure analyte concentrations, analyte diffusivities, and reaction kinetics based on the Péclet number of the species under study. H-filters are essentially T-sensors with dual outlets that have the capability of filtering particles by size in a membrane-less configuration. Multi-stream laminar flow also enables microfluidic patterning inside capillaries [27].

Co-laminar microfluidic fuel cells (Fig. 1) are based on the principle of multi-stream laminar flow. In most configurations, one laminar stream contains the fuel, and a second laminar stream contains the oxidant. For the purposes of this discussion, it is useful to

consider the common and relatively straightforward microfluidic fuel cell geometry shown in Fig. 1a. When the fuel and oxidant streams flow in parallel in a single microchannel, the liquid–liquid interface acts as a virtual separator without the need for a membrane. The position of the electrodes on the channel walls is constrained by the width of the co-laminar inter-diffusion zone: in order to prevent fuel and oxidant crossover effects, the electrodes must have sufficient separation from the liquid–liquid interface with consideration of both channel geometry and operational flow rates. The position and orientation of the electrodes also influences fuel utilization as well as ohmic resistance in the channel. To provide ionic charge transport between the electrodes and to close the electrical circuit, both co-laminar streams must have a reasonably high ionic conductivity. This characteristic is normally facilitated by the addition of a supporting electrolyte that contains ions with high mobility such as hydronium and hydroxide ions. The supporting electrolyte also stabilizes the co-laminar flow with respect to electromigration of fuel and oxidant species, since its highly mobile constituents can redistribute themselves quickly and shield the effects of electric fields and electric double-layers in the channel. The ohmic resistance for ionic transport in the channel depends on the average charge-transfer distance between the electrodes (d_{ct}), the cross-sectional area for charge transfer (A_{ct}), and the ionic conductivity (σ), approximated by:

$$R_f = \frac{d_{ct}}{\sigma A_{ct}} \tag{7}$$

A strong supporting electrolyte with high ionic conductivity and a high microchannel with closely spaced electrodes are therefore desired; however, the inter-diffusion width according to Eq. (6) places a lower limit on the electrode spacing. Ohmic resistance in microfluidic fuel cells is generally higher than in membrane-based fuel cells due to a larger separation of the electrodes, although it can be reduced by increasing the concentration of the supporting electrolyte. Ultimately, the choice of supporting electrolyte should be made with consideration of optimum reaction kinetics. The co-laminar configuration allows the composition of the two streams to be chosen independently, thus providing an opportunity to improve reaction rates and cell voltage. Further, the open-circuit voltage of the cell can be increased by tweaking the reversible half-cell potentials by pH modification of individual streams. For example, the reversible reduction potential (E) of the oxygen reduction reaction:

$$O_2 + 4H^+ + 4e^- \leftrightarrow 2H_2O$$

depends on pH according to the Nernst equation [1]:

$$E = E^0 - \frac{RT}{nF} \ln \frac{\prod_{\text{products},i} a_i^{\upsilon_i}}{\prod_{\text{reactants},j} a_j^{\upsilon_j}} = E^0 - \frac{RT}{4F} \ln \frac{1}{a_{O_2}(a_{H^+})^4} \tag{8}$$

where E^0 is the reversible potential at standard state and a the activity of each species ($a = 1$ at standard state), which for aqueous species can be approximated by the concentration. By reducing the pH of the cathodic stream (adding more H^+), the reversible potential of the cathode becomes more positive and thereby yields a larger open-circuit cell voltage.

In the absence of migration effects, reactant transport from the bulk flow to the surface of the electrode takes place by convection/diffusion. Species conservation then takes the form:

$$\nabla \cdot (C_i \bar{u}) = -\nabla \cdot \bar{J}_i + R_i \tag{9}$$

where C_i is the local concentration of species i and R_i is a source term describing the rate of net generation or consumption of species i via homogeneous chemical reactions. Under the infinite dilution assumption, the diffusive flux of species i is given by Fick's law:

$$\bar{J}_i = -D_i \nabla C_i \tag{10}$$

where D_i is the diffusion coefficient of species i in the appropriate medium. Heterogeneous electrochemical reactions at the fuel cell electrodes appear as species flux terms in the boundary conditions of Eq. (9). During fuel cell operation, a concentration boundary layer that depends on channel geometry and flow rate will develop in the channel, starting at the leading edge of the electrode. The maximum current density of a microfluidic fuel cell, assuming rapid electrochemical reactions, is determined by the rate of the convective/diffusive mass transport from the bulk to the surface of the electrode. In the limiting case, i.e. the transport controlled regime, the reactant concentration is zero at the entire surface of the electrode. Scaling laws for microfluidic fuel cell operation in the transport controlled regime are provided by Kjeang et al. [28], based on pseudo-3D flow over a flat plate. More generally, the current density of a microfluidic fuel cell is controlled by a combination of mass transport, electrochemical kinetics, and ohmic resistance.

3. Fabrication

The majority of microfluidic fuel cells developed to date have made use of fabrication methods established previously for electronics and microfluidic chips (for analytical or lab-on-chip applications). Typically, these devices consisted of a microchannel, two electrodes, and a liquid-tight support structure as shown schematically in Fig. 1a–c. Microchannels were typically fabricated by rapid prototyping, using standard photolithography and soft lithography protocols [29–31]. For microfluidic fuel cell devices with side-by-side streaming (Fig. 1a–c), the channel structures were commonly molded in poly(dimethylsiloxane) (PDMS) and subsequently sealed to a solid substrate that accommodated the electrode pattern. Detailed channel fabrication procedures are available in several reports, for example Kjeang et al. [32]. The common, soft lithography-based procedure is summarized as follows: a pretreated substrate such as a microscope glass slide or a silicon wafer is covered by a thin layer of photoresist during an initial spin-coating step. The rotational speed and duration of the spin-coating program and material properties of the photoresist determine the thickness of the layer, which in turn determines the height of the final microchannel. The coated substrate is soft baked on a hot plate to stabilize the photoresist. A photomask that defines the desired channel structure is drafted in CAD software and printed on a transparency by a high-resolution image setter. The substrate, aligned under the photomask, is then exposed to collimated UV light. After a short post-exposure bake, the unexposed parts of the photoresist are removed by immersion of the substrate in developer liquid. The result is a re-usable master with a positive pattern defined by the remaining polymerized photoresist ridges. The channel structure is fabricated by replica molding in a soft polymer such as PDMS by pouring a liquid mixture of pre-polymer and curing agent over the master, followed by degassing in vacuum, and curing on a hot plate. Upon solidification, the polymer part containing a negative imprint of the channel structure is cut from the mold and removed from the master. The obtained channel structure is sealed to a substrate, typically glass or PDMS, either reversibly as is, or irreversibly following plasma-treating of both parts. Plasma-treating also renders the channel walls hydrophilic, which is useful for microfluidic fuel cells to promote wetting and reduce pressure drop in the channel. PDMS generally has benign properties for fuel cell applications; it is relatively inert and compatible with most solvents and electrolytes [33]. Channel structures can also be fabricated by photolithographic

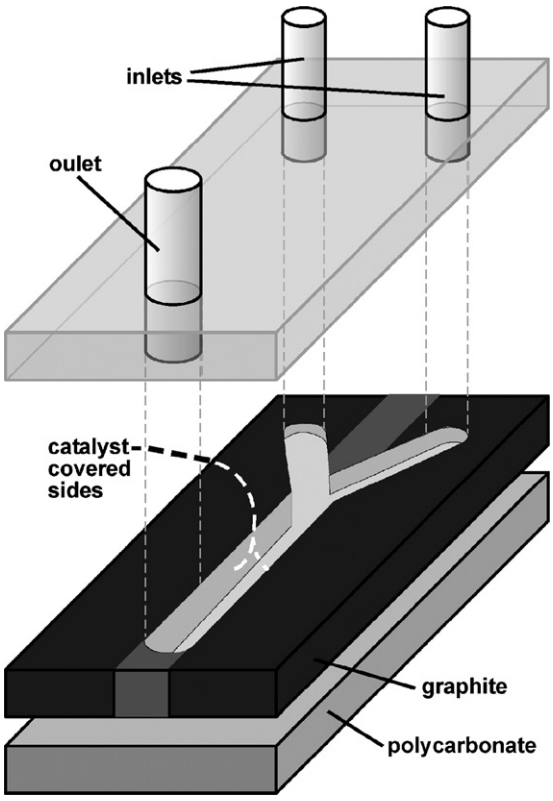

Fig. 2. Sandwich assembly of a microfluidic fuel cell [36]: two machined graphite plates are aligned horizontally and sealed on the top and bottom with PDMS films and polycarbonate capping layers, respectively, to form a microfluidic channel with side-by-side streaming. The graphite plates provide electrode surfaces on the side walls of the obtained microfluidic fuel cell. Reproduced with permission from Choban et al. [36]. Copyright Elsevier (2005).

techniques directly in the photoresist material [34,35]. In this case, a negative relief of the channel structure is desired. Alternatively, four separate parts, each contributing one channel wall, may be assembled into a microfluidic channel. This method was employed by Choban et al. [36,37] to create electrode surfaces on the side walls of a microfluidic channel with side-by-side streaming (Fig. 1b). Two graphite plates were aligned using separators (spacers) and sealed on the top and bottom with PDMS films and polycarbonate capping layers, as shown in Fig. 2; the width and height of the obtained rectangular channel were defined by the separator width and graphite plate thickness, respectively. The number of required parts may be reduced to three by the fabrication of a channel stencil, which has an open area defining the channel along with its two side walls. The stencil approach is particularly useful for microfluidic fuel cells employing vertically layered streaming, given that top and bottom walls are provided by electrode substrates (anode and cathode). The minimum height of a channel stencil is however restricted by the geometry and the stiffness of the material. Channel stencils of ~1 mm height can be fabricated in PDMS by pressing a solid plate against the ridge pattern on the master during curing of the liquid polymer. Another polymeric material frequently employed for microfluidic fuel cell fabrication is poly(methylmethacrylate) (PMMA), often used as an impact resistant substitute for glass. The air-breathing cells developed by Jayashree et al. [38,39] contained a 1-mm high PMMA stencil glued to a graphite plate anode and a Toray carbon paper-based gas diffusion cathode on the top and bottom surfaces, respectively. Li et al. [40] demonstrated a PMMA channel stencil with microstructures engraved using an infrared CO_2 laser. Laser-micromachining enables precise control

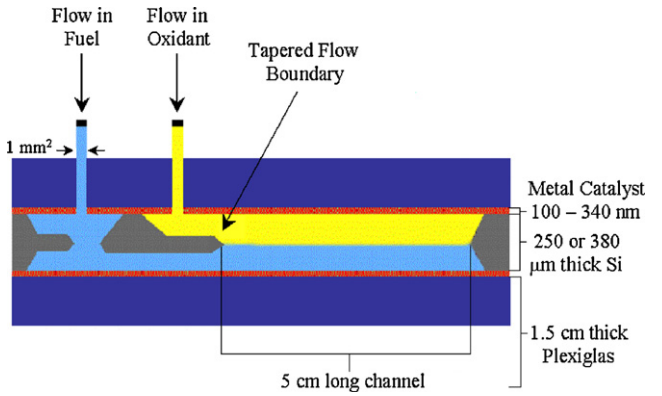

Fig. 3. Microfluidic fuel cell device etched in silicon using a photolithographic procedure [42]. The obtained silicon stencil, coated with an insulator material to prevent electrical short-circuiting, was sealed between two catalyst-coated Kapton® (polyamide) films supported by Plexiglas plates. Reproduced with permission from Cohen et al. [42]. Copyright Elsevier (2005).

of the geometry by adjusting the speed and power of the laser beam. The PMMA stencil was bound between two top and bottom PMMA parts using adhesive gaskets that were also cut to size by the laser. Electrodes were formed prior to assembly by gold sputtering on the top and bottom PMMA parts, mechanically roughened with fine sandpaper to promote adhesion. Microchannel stencils for microfluidic fuel cells have also been produced by silicon etching [41,42], employing a standard photolithography process. A silicon-based microfluidic fuel cell developed by Cohen et al. [42] is shown in Fig. 3. In summary, a silicon wafer was coated with a layer of positive photoresist. The channel pattern was stripped from the photoresist layer by a photolithographic procedure, and a negative relief was obtained in the silicon wafer by etching in potassium hydroxide solution at 90 °C. The height of the produced microchannel, i.e. the depth of the etched pattern, depends on the duration of the etching step. In this case, the etching was continued until the entire thickness of the silicon wafer was penetrated. The obtained silicon stencil, coated with an insulator material to prevent electrical short-circuiting, was sealed between two flexible Kapton® (polyamide) electrode films. A detailed description of this process is provided in Cohen et al. [42].

Most microfluidic fuel cell devices employing side-by-side streaming had electrodes positioned in parallel on the bottom wall. The bottom substrate was typically a glass plate, subject to electrode patterning by two different approaches, both supported by photolithography: lift-off and etch. The lift-off approach utilizes a photoresist layer on the substrate with a negative imprint of the electrode pattern. The substrate is then coated with a conductive material such as graphite, gold or platinum over an adhesive layer of chromium or titanium by standard evaporation or sputtering techniques. The micro-patterned electrodes are obtained by removing the photoresist layer (lift-off) from the fully coated substrate. The etch approach utilizes a similar strategy: the substrate is first coated with a conductive layer, and subsequently covered by a photoresist layer, this time with a *positive* imprint of the electrode pattern. This is followed by an etching step that removes the conductive material, except for the electrode pattern covered by photoresist. Finally, the remainder of the photoresist is removed to uncover the obtained electrodes. A commercial pre-fabricated gold slide can be utilized together with the etch approach as an alternative to the evaporation or sputtering processes [32]. Rigid, self-contained electrode structures such as graphite rods [28] and carbon paper strips [43–45] have also been employed as combined electrodes and current collectors in cells with side-by-side streaming, mounted in parallel

on the bottom channel wall in a PDMS layer with custom shaped grooves or embossed in a polyurethane layer.

The surface area (roughness factor) of the electrode patterns utilized in microfluidic fuel cells was frequently enlarged by electrodeposition of a first or additional layer of conductive material and/or catalyst [32,34,35,46–48]. The same result was achieved by deposition of nanoparticle-supported catalyst suspended in a Nafion-based ink solution applied by pipette or wet sprayed on the electrode, followed by solvent evaporation [36–39]. Other catalyst deposition techniques employed for microfluidic fuel cell electrodes include electron-beam evaporation [35,41,42,47,48], sputtering [49,50], and micromolding [51].

The most common way to accomplish a liquid-tight seal during operation of a microfluidic fuel cell is to physically clamp the assembled parts together using Plexiglas or aluminum plates. This approach has the advantage of facile exchange of parts, which is useful for proof-of-concept studies; however, the use of a clamping device requires additional parts and space. Alternatively, an irreversible seal that does not require clamping is obtained between PDMS/PDMS or PDMS/glass by plasma-treating of both parts prior to assembly [32,43,44,52]. The pressure-driven laminar flow required for operation of a microfluidic fuel cell was typically driven by a syringe pump interfaced via polyethylene tubing. Access holes for inlets and outlets were punched, drilled, or machined in the top part of the microfluidic chips before sealing of the parts.

4. Contributions

Since the invention in 2002, the field of microfluidic fuel cells has generated an array of scientific publications and the technology is now being developed commercially by a US company (INI Power Systems, Morrisville, NC) with core technology licensed from the University of Illinois at Urbana-Champaign. As summarized in Table 1, proof-of-concept microfluidic fuel cell devices have been demonstrated based on hydrogen [41,47,48], methanol [35–38], formic acid [32,39,40,42,43,46,52,53], hydrogen peroxide [50] and vanadium redox species [28,34,44,45] as fuel. Microfluidic bioanodes, for integration in biofuel cells, have also been demonstrated based on ethanol [51] and glucose [49,54] fuel. Oxygen [36–42,46–49,51,54], either in aqueous or gaseous form, is the most commonly used oxidant so far, followed by hydrogen peroxide [32,35,40,50], vanadium redox species [28,34,44,45], potassium permanganate [46,52,53], and sodium hypochlorite [43]; all of which were employed in aqueous media. Ionic charge transport within the fuel and oxidant streams was facilitated by various supporting electrolytes; typically a strong acid or a strong base, such as sulfuric acid and potassium hydroxide, containing highly mobile hydronium or hydroxide ions, respectively. In most cases, the supporting electrolyte was passive and did not participate in the overall cell reaction. The majority of the microfluidic fuel cell devices employed a Y or T-shaped microchannel design featuring two aqueous co-laminar streams of fuel and oxidant dissolved in a supporting electrolyte and catalyst-coated electrodes positioned on the channel walls. There are two possible co-laminar flow configurations with respect to cell design: (i) side-by-side streaming with vertical liquid–liquid interface; and (ii) vertically layered streaming with horizontal liquid–liquid interface. Cells employing side-by-side streaming had T, Y, Ψ or H-shaped microchannels with electrodes positioned either in parallel on the bottom wall (Fig. 1a and c), or on opposite side walls (Fig. 1b). For cells using vertically layered streaming, the channels were F-shaped with electrodes positioned on the top and bottom walls (Fig. 1d and e). In the case of substantially selective catalysts and stable reactants that do not react with each other, a co-laminar flow is however not required to prevent crossover effects and the fuel and oxidant species can be mixed in a single I-shaped stream [35,49,51].

The measured performance characteristics of the microfluidic fuel cells reported to date are summarized in Table 2 based on open-circuit cell voltage, current density, power density, overall power output, and fuel utilization. One of the first microfluidic fuel cells based on co-laminar flow was demonstrated by Choban et al. [46] in 2002. This microfluidic device employed an aqueous fuel stream containing formic acid and an aqueous oxidant stream saturated with oxygen gas, in a Y-shaped microchannel with Pt-coated electrodes integrated on opposite side walls. This proof-of-concept microfluidic fuel cell laid the foundation for significant further work in the field. The power density of the cell was, however, significantly restricted by the rate of mass transport to the active sites, primarily in the cathodic half-cell, and the overall system performance suffered from low fuel utilization. The cathodic transport limitation was demonstrated by switching to potassium permanganate oxidant. Due to the significantly higher solubility in aqueous media, an order of magnitude higher power density was achieved [46]. The high-conductivity liquid electrolyte employed in this type of microfluidic fuel cell enables the use of an external reference electrode to characterize individual half-cells and measure ohmic resistance *in situ* during fuel cell operation. Using this experimental approach, the overall cathodic mass transport limitation of dissolved oxygen-based systems was unambiguously verified [37]. For early devices using formic acid in the anodic stream and dissolved oxygen in the cathodic stream, the measured power density levels were only about 0.2 mW cm^{-2} [42,46], primarily constrained by the low solubility (1–4 mM) and diffusivity (2×10^{-5} cm^2 s^{-1}) of oxygen in the aqueous electrolyte and by CO-poisoning of the Pt catalyst used for formic acid oxidation. By implementing bimetallic Pt/Ru nanoparticles for methanol oxidation that are less susceptible to CO-poisoning, largely improved power densities up to 2.8 mW cm^{-2} were obtained [37]. The nanoparticle-based catalysts also had a very high electrocatalytic surface area (roughness factor of ~500) that further promoted the electrochemical kinetics of both electrodes. Alternatively, adatoms of Bi can be adsorbed on Pt to reduce CO-poisoning. This approach was demonstrated by Cohen et al. [42] in a formic acid/dissolved oxygen co-laminar fuel cell, resulting in drastically improved performance and durability. The fuel cell had a unique F-shaped microchannel design, as depicted in Fig. 3 (also in Fig. 1d), with vertically layered co-laminar streams and relatively large electrodes situated on the top and bottom walls, which is advantageous in terms of overall power output and space-efficient stacking of multiple cells [42].

The combination of gaseous reactants and poly(dimethylsiloxane) (PDMS) material provides an interesting opportunity for microfluidic fuel cell fabrication and design, attributed to the relatively high permeability and solubility of gas in PDMS [55]. This feature enables gaseous reactant supply through thin layers of PDMS to a pair of electrodes separated by an electrolyte channel [47,48]. The power densities of the hydrogen/oxygen [47] and hydrogen/air [48] fuel cells based on this concept (~0.7 mW cm^{-2}) were restricted by the permeation rate of hydrogen through the polymer and by quite severe crossover effects in the absence of electrolyte flow.

4.1. Mixed media operation

In contrast to traditional types of fuel cells operating under all-acidic or all-alkaline conditions, the co-laminar microfluidic fuel cell format enables mixed media operation. This feature provides an opportunity of independently tailored half-cell conditions for optimum reaction kinetics and enhanced cell potential. Cohen et al. [41] demonstrated that the open circuit potential of a hydro-

Table 1
Overview of microfluidic fuel cell devices demonstrated to date.

Reference	Reactants (anode and cathode)	Electrolyte	Catalyst (anode and cathode)	Channel design (W/H/L)	Electrode positions	Features
Ferrigno et al. [34]	Vanadium (II) redox species (1 M) Vanadium (V) redox species (1 M)	Sulfuric acid (25%)	None	Co-laminar Y-shape 2 mm/0.05 or 0.2 mm/17 mm	Bottom wall	3-cell planar array
Choban et al. [46]	Formic acid (2.1 M) Oxygen (aq; sat.) or Potassium permanganate (0.144 M)	Sulfuric acid (0.5 M)	Pt black Pt black	Co-laminar Y-shape 0.5 or 1 mm/0.5 or 1 mm/30 mm	Side walls	
Choban et al. [36]	Methanol (1 M) Oxygen (aq; sat.)	Sulfuric acid or Potassium hydroxide (1 M)	Pt/Ru nanoparticles Pt black nanoparticles	Co-laminar Y-shape 0.75 mm/1 mm/29 mm	Side walls	Mixed media operation
Choban et al. [37]	Methanol (1 M) Oxygen (aq; sat.)	Sulfuric acid (0.5 M)	Pt/Ru or Pt nanoparticles Pt nanoparticles	Co-laminar Y-shape 0.5 or 1 mm/1 mm/29 mm	Side walls	
Mitrovski et al. [47]	Hydrogen Oxygen	Sulfuric acid (0.1 M) or Sodium hydroxide (0.1 or 1 M)	Pt Pt	Passive electrolyte 0.2 mm/0.07 mm/20 mm	Bottom wall	Gas permeation through PDMS
Mitrovski and Nuzzo [48]	Hydrogen Air	Sulfuric acid (5 M) or Sodium hydroxide (2.5 M)	Pd/Pt Pt	Passive electrolyte 0.2 mm/0.07 mm/20 mm	Bottom wall	Gas permeation through PDMS
Cohen et al. [42]	Formic acid (0.5 M) Oxygen (aq; sat.)	Sulfuric acid (0.1 M)	Pt Pt	Co-laminar F-shape 0.38 mm/1 mm/50 mm	Top/bottom walls	Stackable microchannels
Cohen et al. [41]	Hydrogen (aq; sat) Oxygen (aq; sat.)	Potassium hydroxide (0.1 M) or Sulfuric acid (0.1 M)	Pt Pt	Co-laminar F-shape 0.38 mm/1 mm/50 mm	Top/bottom walls	Stackable microchannels
Jayashree et al. [39]	Formic acid (1 M) Air	Sulfuric acid (0.5 M)	Pd black nanoparticles Pt black nanoparticles	Co-laminar F-shape 2 mm/3 mm/20.5 mm	Top/bottom walls	Air-breathing cathode
Jayashree et al. [38]	Methanol (1 M) Air	Sulfuric acid (0.5 M) or Potassium hydroxide (1 M)	Pt/Ru Pt	Co-laminar F-shape 2 mm/3 mm/22 mm	Top/bottom walls	Air-breathing cathode
Hasegawa et al. [50]	Hydrogen peroxide (0.75 M) Hydrogen peroxide (0.75 M)	Sodium hydroxide (0.75 M) Sulfuric acid (0.375 M)	Pt Pt	Co-laminar H-shape 1 mm/0.05 mm/∼10 mm	Bottom wall	
Li et al. [40]	Formic acid (0.5 M) Oxygen (aq; sat.) or Hydrogen peroxide (0.01 M)	Sulfuric acid (0.1 M)	Pt/Ru black Pt black	Co-laminar F-shape 1 mm/1 mm/50 mm	Top/bottom walls	Laser-machined
Sun et al. [52]	Formic acid (2.1 M) Potassium permanganate (0.144 M)	Sulfuric acid (0.5 M)	Pt Pt	Co-laminar Ψ-shape 0.5 mm/0.05 mm/20 mm	Bottom wall	3 co-laminar streams; central blank electrolyte stream

Table 1 (*Continued*)

Reference	Reactants (anode and cathode)	Electrolyte	Catalyst (anode and cathode)	Channel design (W/H/L)	Electrode positions	Features
Kjeang et al. [32]	Formic acid (1–M) Hydrogen peroxide (1–3 M)	Phosphate (1–3 M; pH 6–8) Phosphate (1–2 M; pH 0–1)	Pd Pd or Pt	Co-laminar T-shape 2 mm/0.07–0.17 mm/10 mm	Bottom wall	Grooved microchannel
Kjeang et al. [28]	Vanadium(II) redox species (1–2 M) Vanadium(V) redox species (1–2 M)	Sulfuric acid (1–2 M)	None	Co-laminar Y-shape 2 mm/0.05–0.15 mm/33 mm	Bottom wall	Graphite rod electrodes; 12-cell 3-D array
Kjeang et al. [45]	Vanadium(II) redox species (2 M) Vanadium(V) redox species (2 M)	Sulfuric acid (2 M)	None	Co-laminar Y-shape 2 mm/0.12 mm/27 mm	Bottom wall	Porous electrodes
Kjeang et al. [44]	Vanadium(II) redox species (2 M) Vanadium(V) redox species (2 M)	Sulfuric acid (4 M)	None	Co-laminar T-shape 3 mm/0.15–0.3 mm/12 mm	Bottom wall	Porous flow-through electrodes
Kjeang et al. [43]	Formic acid (1.2 M) Sodium hypochlorite (0.67 M)	Sodium hydroxide (2.8 M)	Pd Au or Pd	Co-laminar T-shape 3 mm/0.3 mm/12 mm	Bottom wall	Porous flow-through electrodes
Salloum et al. [53]	Formic acid (0.04 M) Potassium permanganate (0.01 M)	Sulfuric acid (0.5–1 M)	Pt Pt	Sequential radial flow Circular shape 25.4 mm diameter	Bottom wall	Porous flow-through concentric electrodes
Sung and Choi [44]	Methanol (2 M) Hydrogen peroxide (0.05 M)	Potassium hydroxide (0.2 M)	Nickel hydroxide Silver oxide	Single stream I-shape 0.1 mm high	Bottom wall; interdigitated	Mixed reactants
Moore et al. [51]	Ethanol (1 mM) and NAD^+ (1 mM) Oxygen (aq)	Phosphate (pH 7.15)	Alcohol dehydrogenase enzyme Pt	Single stream I-shape 0.2 mm/0.1 mm/25 mm	Bottom wall	Bioanode; mixed reactants
Togo et al. [49]	Glucose (5 mM) and NAD^+ (1 mM) Oxygen (aq; air sat.)	Phosphate (50 mM; pH 7.0) and sodium chloride (0.1 M)	Diaphorase and glucose dehydrogenase enzymes Pt	Single stream I-shape 3 mm wide/1 mm high	Bottom wall	Bioanode; mixed reactants
Togo et al. [54]	Glucose (10 mM) and NAD^+ (1 mM) Oxygen (aq; air sat.)	Phosphate (50 mM; pH 7.0) and sodium chloride (0.1 M)	Diaphorase and glucose dehydrogenase enzymes Bilirubin oxidase enzyme	Single stream I-shape 3 mm wide/0.1–1 mm high	Bottom wall	Biofuel cell; mixed reactants

Table 2
Room-temperature performance of microfluidic fuel cell devices demonstrated to date.

Reference	Fuel	Oxidant	Max cell voltage (V)	Max current density (mA cm^{-2})	Max power density (mW cm^{-2})	Max power output (mW)	Max fuel utilization
Unit cells							
Ferrigno et al. [34]	V^{2+}	VO_2^+	1.59	80	38	3.2	~10%
Choban et al. [46]	HCOOH	O_2	0.7	0.8	0.17	0.05	<1%
	HCOOH	$KMnO_4$	1.1	8	2.4	0.7	<1%
Choban et al. [36]	CH_3OH	O_2	1.4	40	12	–	<10%
Choban et al. [37]	CH_3OH	O_2	0.7	8	2.8	–	<15%
Mitrovski et al. [47]	H_2	O_2	1.0	1.6	0.7	0.01	–
Mitrovski and Nuzzo [48]	H_2	Air	1.0	1.2	0.7	0.01	–
Cohen et al. [42]	HCOOH	O_2	0.64	1.5	0.18	0.045	–
Cohen et al. [41]	H_2	O_2	1.45	0.85	0.75	0.38	–
Jayashree et al. [39]	HCOOH	Air	0.9	130	26	16	33%
Jayashree et al. [38]	CH_3OH	Air	1.05	120	17	11	–
Hasegawa et al. [50]	H_2O_2	H_2O_2	0.7	76	23	0.6	–
Li et al. [40]	HCOOH	O_2	0.75	1.5	0.58	0.29	–
	HCOOH	H_2O_2	0.65	7.2	2.0	1.0	–
Sun et al. [52]	HCOOH	$KMnO_4$	1.0	2.6	0.7	0.03	–
Kjeang et al. [32]	HCOOH	H_2O_2	1.1	150	30	1.5	–
Kjeang et al. [28]	V^{2+}	VO_2^+	1.46	92	35	5.8	63%
Kjeang et al. [45]	V^{2+}	VO_2^+	1.38	243	70	7.6	55%
Kjeang et al. [44]	V^{2+}	VO_2^+	1.55	326	131	16	100%
Kjeang et al. [43]	HCOOH	NaOCl	1.42	230	52	6.2	100%
Salloum et al. [53]	HCOOH	$KMnO_4$	1.2	5	2.8	12	58%
Sung and Choi [44]	CH_3OH	H_2O_2	0.11	1.1	0.03	4e−4	–
Moore et al. [51]	Ethanol	O_2	0.34	0.05	0.005	7e−5	–
Togo et al. [49]	Glucose	O_2	0.55	0.13	0.03	0.001	–
Togo et al. [54]	Glucose	O_2	0.8	0.16	0.07	0.02	–

Reference	Fuel	Oxidant	Max cell voltage (V)	Max current density (mA cm^{-2})	Max power density (mW cm^{-2})	Max power output (mW)	Max fuel utilization	Number of cells
Arrays and stacks								
Ferrigno et al. [34]	V^{2+}	VO_2^+	1.46	–	–	–	–	3
Cohen et al. [42]	HCOOH	O_2	0.73	–	–	0.4	–	5
Cohen et al. [41]	H_2	O_2	1.44	–	0.48	1.2	–	5
Kjeang et al. [28]	V^{2+}	VO_2^+	1.36	12	3.8	28	78%	12

gen/oxygen fuel cell can be raised well beyond the standard cell potential of 1.23 V by implementation of an alkaline dissolved hydrogen stream and an acidic dissolved oxygen stream in a co-laminar microfluidic fuel cell of the previously reported F-shaped architecture (Fig. 3) [42]. The increased cell potential is established by the negative shift of the hydrogen oxidation potential experienced in alkaline environments. The power produced in the dual electrolyte configuration was more than twice that for the corresponding single electrolyte systems, despite the relatively slow kinetics of the hydrogen oxidation reaction in alkaline media. The overall performance was however still restricted by the transport limitations associated with the low gas solubility. The media flexibility was also explored by Choban et al. [36] by operating a methanol/oxygen fuel cell under all-acidic, all-alkaline, and mixed media conditions. In contrast to conventional direct methanol fuel cells, the microfluidic fuel cell design eliminated the issue of membrane clogging by carbonate products formed in alkaline media. Alkaline conditions had positive effects on the reaction kinetics at both electrodes, while the cell potential was increased under mixed media conditions (alkaline anolyte and acidic catholyte) up to an impressive 1.4 V. The methanol/oxygen fuel cell produced a peak power density of 5 mW cm^{-2} at 1.0 V cell voltage under mixed-media conditions, compared to 2.4 and 2.0 mW cm^{-2} for all-acidic and all-alkaline conditions, respectively. Another interesting phenomenon was observed in this study: at cell voltages below 0.8 V, the oxygen reduction reaction at the cathode was complemented by proton reduction to hydrogen, thereby providing an additional contribution to the cathodic mass transport controlled cell current. This phenomenon is a direct consequence of the mixed media configuration and would not occur in a single electrolyte system. The combined current from the oxygen reduction and proton reduction reactions enabled significantly enhanced fuel cell performance with a peak power density of 12 mW cm^{-2}. Hasegawa et al. [50] used the mixed media approach to operate a microfluidic fuel cell on hydrogen peroxide as *both* fuel and oxidant, in alkaline and acidic media, respectively. The proof-of-concept direct hydrogen peroxide fuel cell produced relatively high power densities up to 23 mW cm^{-2}, partially constrained by the rate of spontaneous hydrogen peroxide decomposition on the cathode and associated oxygen gas evolution that may perturb the co-laminar flow interface.

Operation under mixed media conditions, however, causes exothermic neutralization of OH^- and H^+ at the co-laminar flow interface resulting in the formation of a liquid junction potential and locally reduced ionic strength that may have negative effects on both cell potential and ohmic cell resistance. Furthermore, in all three cases described above, the overall cell reaction included net consumption of supporting electrolyte, i.e. protons at the cathode and hydroxide ions at the anode. The consumption of supporting electrolyte must be taken into account when considering the overall energy density of the fuel cell system. For example, the theoretical energy density of the mixed media methanol/oxygen cell is only one-fifth of the corresponding all-acidic and all-alkaline cells that only consume methanol [36].

4.2. Air-breathing cathodes

One way to address the oxygen solubility limitation is to integrate an air-breathing porous cathode structure that allows gaseous oxygen transport from the ambient air, a source of oxygen that has

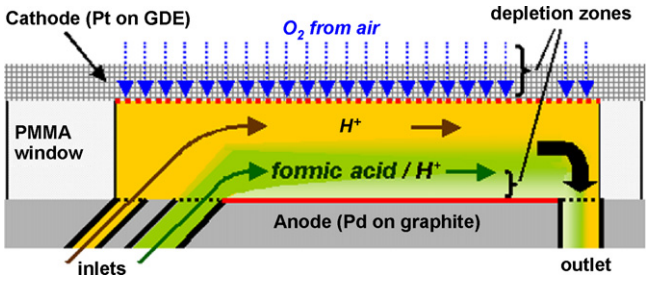

Fig. 4. An air-breathing microfluidic fuel cell captures oxygen from the surrounding air via gas diffusion through the 'dry' side of the porous cathode structure. The opposite 'wet' side is in contact with a blank electrolyte stream, establishing a three-phase interface between the gas, electrolyte, and catalyst/solid electrode phases. Reprinted with permission from Jayashree et al. [39]. Copyright 2005 American Chemical Society.

four orders of magnitude higher diffusivity ($0.2\,cm^2\,s^{-1}$) and several times higher concentration (10 mM) than dissolved oxygen in aqueous media [39]. Similar gas diffusion electrodes are key components for PEM-based fuel cell designs, where they provide high levels of current density. Jayashree et al. [39] introduced the first microfluidic fuel cell with integrated air-breathing cathode, using a graphite plate anode covered with Pd black nanoparticles and a porous carbon paper cathode covered with Pt black nanoparticles, shown in Fig. 4 (also in Fig. 1e). The air-breathing cell architecture requires a blank cathodic electrolyte stream to provide sufficient separation between the inter-diffusion zone and the cathode, and to facilitate ionic transport to the cathodic reaction sites. A peak power density of $26\,mW\,cm^{-2}$ was achieved with 1 M formic acid in 0.5 M sulfuric acid anolyte and a blank 0.5 M sulfuric acid catholyte flowing at $0.3\,mL\,min^{-1}$ per stream. The air-breathing cell architecture was also evaluated using methanol [38], a fuel that enables higher overall energy density than formic acid. Despite the modest power densities obtained with 1 M methanol fuel ($17\,mW\,cm^{-2}$), this study demonstrated significantly improved reaction kinetics for both methanol oxidation and oxygen reduction by switching from an acidic to an alkaline supporting electrolyte, while raising the open-circuit cell voltage from 0.93 to 1.05 V in the absence of methanol crossover. The air-breathing cells also enabled significantly higher coulombic fuel utilization than the cells based on dissolved oxygen, up to a maximum 33% per single pass at a reduced flow rate of $0.1\,mL\,min^{-1}$ [39]. The air-breathing requirement, however, can complicate the scale-up of these systems, and in addition, these cells would also require a recirculation scheme to achieve high fuel utilization and high overall energy conversion efficiency. Direct methanol microfluidic fuel cells with integrated gas diffusion cathode are currently being developed towards commercial applications by INI Power Systems (Morrisville, NC), under the registered trademark "Laminar Flow Fuel Cell (LFFC®)". Further improvements of electrodes and catalysts, optimization of methanol concentration and flow rates, and the addition of a gaseous flow field on the cathode side have resulted in power densities on the order of $100\,mW\,cm^{-2}$ [56], which are quite competitive compared to other types of direct methanol fuel cells [3].

4.3. Liquid oxidants

The use of alternative oxidants soluble at higher concentrations than dissolved oxygen provides another avenue towards improved performance of typically mass transfer-limited microfluidic fuel cells. With respect to fuel and oxidant selection, there are many liquid fuels available with high specific energy density, including sodium borohydride, methanol, formic acid and other liquid hydrocarbons [3,4,6]. Conventional fuel cells based on these fuels are normally coupled with oxygen or air cathodes. Liquid oxidants are less common, except for hydrogen peroxide, which was previously employed as an oxidant in various direct sodium borohydride/hydrogen peroxide fuel cells [57–59] with traditional PEM-based design. Unless the fuel cell system is targeted at applications in anaerobic conditions (e.g. space or underwater applications), the use of a liquid oxidant is associated with a reduced system energy density that must be compensated by significant performance gains or other important system improvements.

An acidic hydrogen peroxide solution was employed as the oxidant in a laser-micromachined microfluidic fuel cell device [40] together with formic acid fuel in an F-shaped co-laminar format, demonstrating power densities up to $2\,mW\,cm^{-2}$ for operation at flow rates of $0.4–1.6\,mL\,min^{-1}$ per stream. The performance of this cell was primarily restricted by the low hydrogen peroxide concentration (10 mM). Direct hydrogen peroxide reduction on common catalysts such as Pt and Pd is however accompanied by vigorous oxygen gas evolution from parasitic oxidation (decomposition) that must be accommodated by strategic cell design without compromising the stability of the co-laminar flow. Three methods to stabilize the co-laminar liquid–liquid interface have recently been proposed: magnetically separated streams [60], integration of a third electrolyte stream [52], and utilization of a grooved microchannel geometry [32]. Aogaki et al. [60] reported a magnetic field-induced virtual wall that separated a paramagnetic oxidant solution from a diamagnetic fuel solution at a liquid–liquid interface. This novel concept was demonstrated in a zinc/copper flow cell configuration supported by a permanent magnet. The self-adjustable and self-reformable properties of the magnetic channel enable rapid removal of bubbles and solid particles, and precise crossover control. A Ψ-shaped microfluidic fuel cell was demonstrated by Sun et al. [52], incorporating a third electrolyte stream in the centre of the co-laminar flow channel. The purpose of the third stream, containing blank electrolyte, was to promote the separation of the fuel and oxidant streams and prevent interfacial reaction. During cell operation on formic acid and potassium permanganate, both cell voltage and current density could be optimized via precise flow rate control of the central electrolyte stream. Kjeang et al. [32] recently reported a microfluidic fuel cell running on formic acid and hydrogen peroxide, exploiting a grooved microchannel design. The high channel parts situated directly above the electrodes effectively captured all gas bubbles formed by the electrochemical reactions while stabilizing the co-laminar flow. This unique capability enabled steady operation without crossover issues at flow rates as low as $3\,\mu L\,min^{-1}$, and practical power densities up to $30\,mW\,cm^{-2}$ were achieved.

Gold has been identified as an alternative catalyst for hydrogen peroxide reduction that minimizes gas evolution while providing high current density [61], which could be useful for microfluidic fuel cells. Gold is also a suitable catalyst for direct borohydride oxidation with limited hydrogen evolution [61], and the end product, sodium metaborate, is highly soluble in aqueous media. However, in contrast to direct borohydride/hydrogen peroxide fuel cells where the anolyte and catholyte are physically separated by a membrane, the feasibility of coupling sodium borohydride and hydrogen peroxide in a microfluidic fuel cell environment is restricted by stability issues: sodium borohydride is only stable in alkaline solutions, and hydrogen peroxide requires an acidic environment to prevent fast decomposition. Mixing of an alkaline borohydride solution with an acidic peroxide solution leads to vigorous gas formation and heat liberation from spontaneous decomposition. A microfluidic fuel cell that couples these two components in a co-laminar flow arrangement is therefore not fea-

sible. Individual half-cells based on either alkaline borohydride or acidic peroxide might, however, find some application in a cell architecture that accommodates low rates of gas evolution, such as the previously described grooved microchannel design [32].

A completely different strategy to circumvent the stability problem associated with hydrogen peroxide oxidant is to employ selective catalysts on both electrodes. In this case, crossover is not a concern at all, and the fuel and oxidant solutions can be mixed in a single laminar stream. The mixed reactant approach is however restricted to fuel and oxidant pairs that do not react spontaneously upon mixing and have sufficiently high kinetics in a singular electrolyte. Sung and Choi [35] demonstrated a single-stream microfluidic fuel cell based on non-noble catalysts in alkaline solution: a nickel hydroxide anode for methanol oxidation and a silver oxide cathode for hydrogen peroxide reduction. These catalysts are not entirely selective and their relatively mild catalytic activity resulted in very low open-circuit voltage (0.12 V) and power density (0.03 mW cm^{-2}). The bottom substrate of the proof-of-concept cell was patterned with interdigitated planar microelectrodes, and it was demonstrated that the output power increased as the spacing of the electrodes was reduced, due to improved transport characteristics.

Established vanadium redox battery technology utilizes soluble vanadium redox couples in both half-cells for large-scale regenerative energy storage units [62]. The same vanadium redox system has also been exploited in a number of microfluidic fuel cell designs; in fact, the first journal publication in the emerging microfluidic fuel cell field was an all-vanadium microfluidic redox fuel cell introduced by Ferrigno et al. in 2002 [34]. Vanadium redox fuel cells utilize two different aqueous vanadium redox couples, V^{2+}/V^{3+} and $VO^{2+}/VO_2{}^+$, as fuel and oxidant, respectively, dissolved in dilute sulfuric acid. This combination of redox pairs offers several advantages for microfluidic fuel cell operation: they provide well-balanced electrochemical half-cells in terms of reaction rates and transport characteristics; they have high solubility and enable relatively high redox concentrations up to 5.4 M [63]; they have a large difference in formal redox potentials resulting in a high open-circuit voltage (up to ~1.7 V at uniform pH); and the reactions are facilitated by bare carbon electrodes without precious metal catalysts. The microfluidic vanadium redox fuel cell developed by Ferrigno et al. [34] employed planar graphite-covered gold electrodes patterned on the bottom wall of a Y-shaped microchannel. When operated at a high flow rate of 1.5 mL min^{-1} per stream, the fuel cell delivered high power densities (38 mW cm^{-2}), but the fuel utilization was limited to ~0.1%. A similar vanadium redox fuel cell was demonstrated by Kjeang et al. [28] based on graphite rod electrodes. Commonly employed as mechanical pencil refills, graphite rods are inexpensive and provide combined electrodes and current collectors in simple self-contained structures. The proof-of-concept fuel cell provided power density levels comparable to those of Ferrigno et al. [34] at high flow rates. Empirical transport analysis verified that the performance was primarily restricted by convective/diffusive species transport from the bulk fluid. In addition, operation at low flow rates was demonstrated with high levels of fuel utilization up to 63% per single pass, mainly attributed to the high-aspect ratio (width/height) cross-sectional geometry of the microchannel. The cell design was improved further by the integration of porous carbon electrodes (Fig. 1c) in place of the graphite rods [45]. The porous electrodes enabled enlarged active surface area and enhanced transport characteristics associated with a small parallel flow inside the top portion of the porous medium, thereby delaying otherwise commonly encountered transport limitations. Based on these improvements, a peak power density of 70 mW cm^{-2} was achieved.

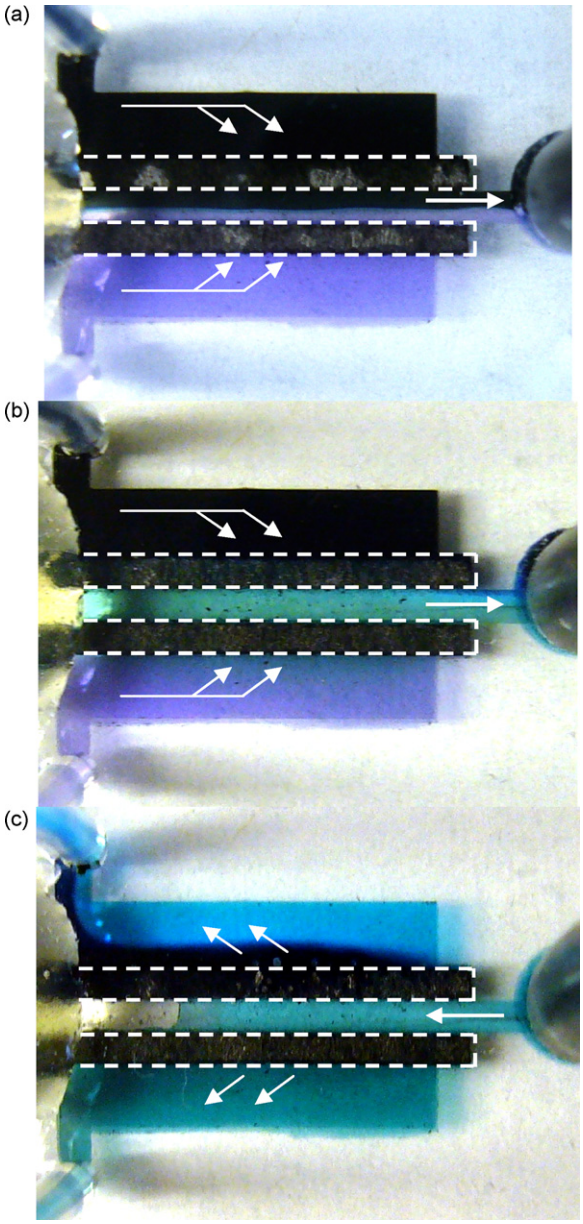

Fig. 5. Annotated images of the flow through porous electrode microfluidic fuel cell in operation at (a) open-circuit and (b) 0.8 V cell voltage. The vanadium electrolytes contain V^{2+} (purple) and V^{3+} (light green) at the anode, and $VO_2{}^+$ (black) and VO^{2+} (turquoise) at the cathode. The flow rate was 1 μL min^{-1} per stream. (c) Image of the fuel cell operating in reverse, demonstrating the *in situ* regeneration capability. Fully mixed waste solution (~50/50 V^{3+}/VO^{2+}) is flowing in the reverse direction from right to left at 1 μL min^{-1} per stream, and an applied cell voltage of 1.5 V. Dashed lines indicate the extent of the porous electrodes, and arrows indicate flow directions. Reproduced with permission from Kjeang et al. [44]. Copyright 2008 American Chemical Society. (For interpretation of the references to colour in this figure legend, the reader is referred to the web version of the article.).

4.4. Flow-through porous electrodes

Kjeang et al. [44] further modified the vanadium redox fuel cell architecture by sealing the porous electrodes between the top and bottom substrates and delivering the reactants via cross-flow through the electrodes. The flow through porous electrode cell is shown schematically in Fig. 1 g, and in operation in Fig. 5. The two reactant streams meet in an orthogonally arranged central channel where they are directed towards the outlet in a co-laminar format. The uniform flow distribution through the entire porous electrodes

enabled utilization of the full depth of the porous medium and associated active area, and provided enhanced species transport from the bulk to the active sites. The various colours inherent to different vanadium solutions enable direct visualization of the fuel cell operation. At open circuit (Fig. 5a), co-laminar streaming of the fuel and oxidant in the waste stream is apparent. In operation at 0.8 V (Fig. 5b), fuel and oxidant are largely consumed in the porous electrode structure prior to reaching the co-laminar waste channel. The flow through porous electrode architecture enabled exceptionally high room-temperature performance levels, including steady state power densities up to 131 mW cm^{-2} and near complete fuel utilization. The fuel cell also had the capability to combine high fuel utilization with high cell voltages. At 1 μL min^{-1} flow rate, for example, an active fuel utilization of 94% per single pass was achieved at 0.8 V, which is equivalent to an overall energy conversion efficiency of 60%. In addition, proof-of-concept *in situ* regeneration of the initial fuel and oxidant species was established by operating the fuel cell in reverse mode. An image of the fuel cell in regeneration mode is given in Fig. 5c. *In situ* regeneration, or recharging, is a unique advantage owing to the combination of the redox system and flow-through architecture employed.

The main trade-off associated with the use of vanadium redox couples in a microfluidic fuel cell system is that the energy density of such a device would ultimately be limited by the solubility of the vanadium redox species. To address this issue, a novel alkaline microfluidic fuel cell system was proposed, based on formate fuel and hypochlorite oxidant [43]. The reactant solutions were obtained from formic acid and sodium hypochlorite, both of which are available and stable as highly concentrated liquids, thereby enabling a fuel cell system with high overall energy density. Formate oxidation and hypochlorite reduction were established in alkaline media on porous Pd and Au electrodes, respectively, showing rapid kinetics at low overpotentials while preventing gaseous CO_2 formation by carbonate absorption. The prototype formate/hypochlorite fuel cell with flow-through porous electrode architecture exhibited a peak power density of 52 mW cm^{-2}, primarily constrained by ohmic resistance, and concurrently achieved high fuel utilization and high cell voltages comparable to those of the preceding vanadium redox fuel cell.

The benefits of flow-through porous electrodes were also demonstrated by Salloum et al. [53] in a sequential flow-based microfluidic fuel cell device with concentric electrodes. This device is shown schematically in Fig. 1 h; anolyte flow enters through the center of a disc-shaped anode and flows radially towards a ring-shaped cathode. The partially consumed anolyte is mixed with catholyte in a small gap section before entering the porous cathode. The concentric cell design enables independent control over the fuel and oxidant flow rate, although the impact of the high fuel crossover rate to the cathode would be severe unless a selective cathode catalyst is utilized.

4.5. Modeling advances

Mathematical and computational modeling is an important tool in the analysis of the transport phenomena and electrochemical reactions that take place inside a microfluidic fuel cell. This area was first investigated by Bazylak et al. [64] using computational modeling to analyze a T-shaped formic acid/dissolved oxygen microfluidic fuel cell with side-by-side streaming. Different cross-sectional channel geometries and electrode configurations were analyzed, targeting enhanced fuel utilization while minimizing fuel/oxidant mixing. The transport processes were solved in 3D using a computational fluid dynamics framework coupled with convective/diffusive mass transport (infinite dilution) and electrochemical reaction rate models for both anode and cathode. It was found that a high aspect ratio (width/height) channel geometry with electrodes placed on the top and bottom walls would enable significantly improved fuel utilization and reduced inter-diffusional mixing width. The numerical study also suggested the implementation of a tapered electrode design that accommodates the growth of the co-laminar mixing zone in the downstream direction, with resulting profile shown in Fig. 6. An extended theoretical/computational model was developed by Chang and co-workers [65,66], extended with Butler–Volmer electrochemical reaction kinetics, with the capability of predicting complete polarization curves. The results obtained for Y-shaped [65] and F-shaped [66] formic acid/dissolved oxygen-based cells were in good agreement with foregoing experimental studies [42,46], and confirmed the cathodic activity and mass transport limitations. Consequently, the predicted cell performance was independent of anodic formic acid concentration. The numerical results also recommended high aspect ratio channel geometry, high Péclet number, high oxygen concentration and a thick cathode catalyst layer to improve the performance. This work was complemented by a 2D theoretical model of the cathode kinetics under co-laminar flow [67], used to study single reaction kinetics of the oxygen reduction reaction and linked simultaneous reaction kinetics considering hydrogen peroxide intermediate product. A Butler–Volmer model [68] was also developed for the microfluidic fuel cell using hydrogen peroxide as both fuel and oxidant in mixed media [50], examining the effects of species transport and geometrical design. In this case, the simulated fuel cell performance was invariant at flow rates above 0.1 mL min^{-1}, indicating the absence of the commonly encountered cathodic transport limitation. It was also found that increasing the surface area and thickness of the catalyst layers can enhance current density, although concentration losses and ohmic resistance must be taken into account. Two-phase flow and transport effects related to oxygen gas evolution from hydrogen peroxide decomposition were not considered in that study.

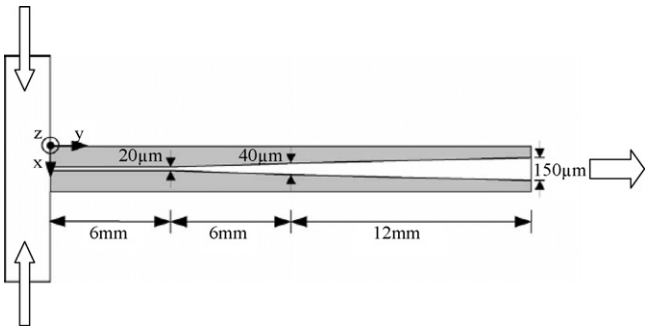

Fig. 6. Schematic of the tapered electrode geometry, designed to maximize fuel utilization while accommodating downstream growth of the inter-diffusion zone in the center of the channel. Reproduced with permission from Bazylak et al. [64]. Copyright Elsevier (2005).

4.6. Boundary layer mitigation

The concentration boundary layers in microfluidic fuel cells can be replenished via strategic design modifications in order to enhance the overall fuel cell performance. Yoon et al. [69] proposed three different strategies for active control of concentration boundary layers, shown in Fig. 7: (i) removing consumed species through multiple periodically placed outlets; (ii) adding reactants through multiple periodically placed inlets; and (iii) generating a secondary transverse flow by topographical herringbone patterns on the channel walls. The benefits of these design modifications were evaluated through simulations and experiments using the ferricyanide/ferrocyanide redox couple as a model system. A

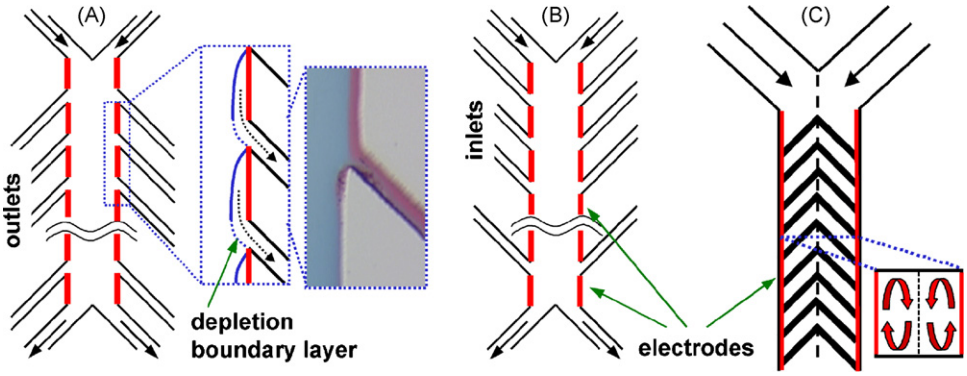

Fig. 7. Three different strategies for active control of concentration boundary layers in microfluidic fuel cells: (a) removing consumed species through multiple periodically placed outlets; (b) adding reactants through multiple periodically placed inlets; and (c) generating a secondary transverse flow by topographical herringbone patterns on the channel walls. Reproduced from Yoon et al. [69] by permission of the Royal Society of Chemistry (RSC).

chronoamperometric study revealed that the transport-controlled current could be enhanced by ~30% when two extra inlets were added, without increasing the overall flow rate. Topographical herringbone ridge patterns, developed by Stroock et al. [70] for microfluidic chaotic mixers and analyzed theoretically by Kirtland et al. [71] for microreactor systems, induce a secondary spiralling flow that enhances the rate of cross-stream transport in microchannels, depending on the exact geometry of the pattern. In this case, a chronoamperometric demonstration showed a 10–40% increase in current density upon addition of herringbone ridges to one wall. For microfluidic fuel cells, this approach is particularly useful towards improved fuel utilization, but must be used cautiously to avoid increased fuel and oxidant mixing at the co-laminar flow interface. Active boundary layer control also has the disadvantage of increased complexity with respect to fluid handling and/or increased parasitic pumping power required to drive the flow. As suggested by Lim and Palmore [72], passive boundary layer control can be achieved by splitting the electrodes into smaller units separated by a gap. Towards this end, a prototype microfluidic redox fuel cell with five sets of consecutive electrodes was fabricated. The local current density at the second set of electrodes was enhanced by the passive replenishment of the concentration boundary layer in the gap section, and a relationship between the measured current density and the distance between consecutive electrodes was developed. However, since the geometrical surface area required for the gap did not contribute any net current, the overall current density of the fuel cell was not improved. This work was followed by a numerical optimization study by Lee et al. [73], recommending arrays of miniaturized electrodes, i.e. nanoelectrodes, provided that short electrodes require a smaller gap for maximum efficiency.

4.7. *Microfluidic biofuel cells*

Many microfluidic fuel cell architectures are also well-suited for use with biological catalysts. Biofuel cells [8,9] utilize biological molecules such as enzymes and microbes to catalyze the chemical reactions, thereby replacing traditional electrocatalysts. Conventionally, biocatalytic entities are placed in a two-compartment electrochemical cell containing buffered solution with concentrated fuel and oxidant in the anolyte and catholyte compartments, respectively. These compartments are generally separated by an ion-exchange membrane or a salt bridge [8]. Each compartment also includes a redox couple acting as a diffusional electron mediator (cofactor), which is necessary for efficient catalyst utilization. The rate of electron transfer is generally confined by the rate of diffusion of these redox species and the ion permeability of the membrane that separates the two compartments [9]. Moreover, enzymes in solution are only stable for a few days. Recently, several novel methodologies have been developed for the functionalization of electrode surfaces and immobilization of active enzymes in order to improve electron transfer characteristics and stability: covalent polymer tethering of cofactor units to multi-layered enzyme array assemblies; cross-linking of affinity complexes formed between redox enzymes and immobilized cofactors on functionalized conductive supports; and non-covalent coupling by hydrophobic/hydrophilic or affinity (e.g. antigen–antibody) interactions [74].

The immobilization of enzymes on conductive supports enables integrated microfluidic biofuel cell designs. Biofuel cells with non-selective electrochemistry, i.e. cells using diffusional redox mediators, can utilize the established co-laminar microfluidic fuel cell design, which also enables the tailoring of independent anolyte and catholyte compositions for optimum enzymatic activity and stability. Full selectivity of both anodic and cathodic half-cells (i.e. co-immobilized redox relays and enzymes based on suitable immobilization schemes with electronic coupling) allows microfluidic biofuel cell operation in a single, combined fuel and oxidant channel with mixed reactants. A microfluidic system would also be favourable for stability studies since the reactant concentrations can be kept constant by continuous flow.

The number of microfluidic biofuel cells presented to date is limited. The area was pioneered by Moore et al. [51], who presented a microchip-based bioanode with NAD-dependent alcohol dehydrogenase enzymes immobilized in a tetrabutylammonium bromide-treated Nafion membrane. The bioanode was assembled on a micromolded carbon electrode integrated on a glass substrate, sealed under a PDMS microchannel that was used to deliver the fuel solution containing ethanol and NAD^+ in phosphate buffer. When operated versus an external platinum cathode, the microfluidic bioanode produced an open-circuit voltage of 0.34 V and a maximum current density of 53 $\mu A\,cm^{-2}$, expected to be limited by the rate of diffusion of NADH within the membrane. This research is continued towards an integrated microfluidic fuel cell based on the unique modified Nafion-based enzyme immobilization technique [75,76]. The technology is currently licensed to Akermin Inc. of St Louis, MO, under the trademark “stabilized enzyme biofuel cells”, which is considered state-of-the-art microfluidic biofuel cell technology in terms of both power density and stability.

Togo et al. [49] developed a microfluidic bioanode based on vitamin K_3-mediated glucose oxidation by the glucose dehydrogenase enzyme. The bioanode was immobilized inside a fluidic chip containing a PDMS-coated conventional Pt cathode and an integrated Ag/AgCl reference electrode. The bioanode was placed downstream of the Pt cathode to minimize the presence of contaminating oxy-

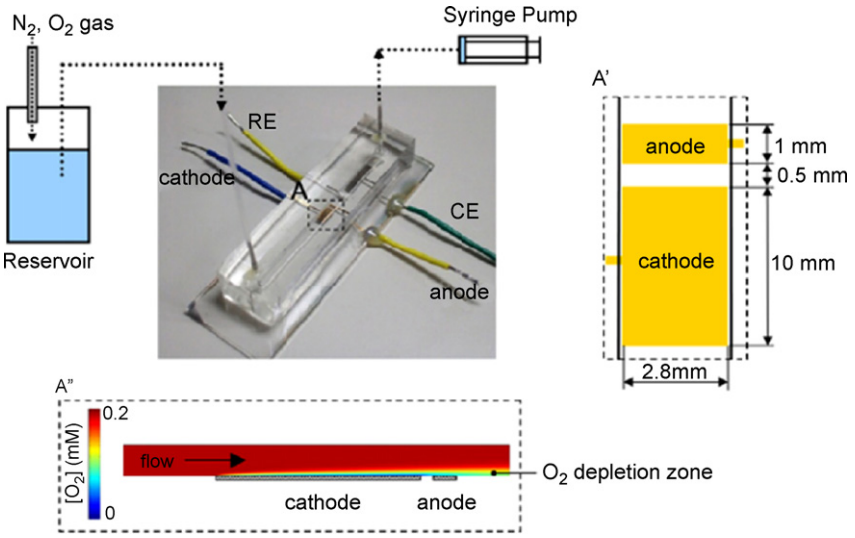

Fig. 8. Schematic of a microfluidic biofuel cell with an upstream biocathode and a downstream bioanode integrated on the bottom channel wall. The biofuel cell was operated using a mixed reactant feed of oxygen-saturated glucose solution. The reaction zone (A) is magnified to show the electrode configuration (A′) and the growth of the oxygen concentration boundary layer formed on the cathode (A″). Reproduced with permission from Togo et al. [54]. Copyright Elsevier (2008).

gen in the anode vicinity. The flow cell produced 32 μW cm^{-2} at 0.29 V when an air-saturated pH 7-buffered fuel solution containing 5 mM glucose and 1 mM NAD^+ was introduced at 1 mL min^{-1} flow rate. The current density of the proof-of-concept cell declined by 50% over 18 h of continuous operation, probably due to swelling effects. In a more recent report from Togo et al. [54], the Pt cathode was replaced with a bilirubin oxidase-adsorbed biocathode. The resulting complete microfluidic biofuel cell is illustrated in Fig. 8. The power output of the biofuel cell was comparable to the previous device. A parametric study of flow rate, channel height and electrode geometry demonstrated restricted access of dissolved oxygen to the biocathode. The present cell design mitigates this limitation by enlarging the cathode area to ten times the anode size.

Strategic patterning of multiple enzyme electrodes to harness consecutive reactions represents a significant opportunity for biofuel cell technologies, particularly with respect to fuel utilization. This opportunity was investigated by Kjeang et al. [77], using a generic computational model of species transport in microchannels coupled with heterogeneous chemical reactions and Michaelis–Menten enzyme kinetics. This was the first computational study of microfluidic biofuel cell technology, and the results were intended to provide guidelines for the design and fabrication of microfluidic biofuel cells exploiting consecutive reactions. Separated and mixed enzyme patterns in different proportions were analyzed for various Péclet numbers. The mixed transport regime (medium Pe) was shown to be particularly attractive while current densities were maintained close to maximum levels. Optimum performance was achieved by mixed enzyme patterning tailored with respect to individual turnover rates, enabling high current densities combined with nearly complete fuel utilization.

4.8. Expanded cell architectures

The majority of microfluidic fuel cell devices reported to date were proof-of-concept unit cells. As shown in Table 2, the cell voltage and overall power output of these unit cells were generally less than 1 V and 10 mW, respectively, which is insufficient for most portable power applications. Microfluidic fuel cell technology can be scaled up based on various expansion methodologies. Ferrigno et al. [34] demonstrated a planar array of three cells with separate inlets and outlets, based on the Y-shaped channel geometry with side-by-side streaming and electrodes positioned on the bottom wall. The array produced roughly three times the power of the unit cell and provided useful operational voltages up to 2.4 V when connected in series. Although planar arrays of this type are convenient from a fabrication perspective, they require substantial "overhead" volume of passive materials that restricts the volumetric power density of the device. Cohen et al. [41,42] reported a more space-efficient planar expansion methodology for parallel microchannels with combined inlets and outlets. The prototype 5-microchannel array employed five parallel 1 mm wide and 5 cm long microchannels of the F-shaped design, using vertically layered streaming, and was operated on aqueous formic acid or hydrogen fuel together with dissolved oxygen in the cathode stream. The measured power output of the array scaled linearly with the results obtained for a single microchannel [42], indicating uniformly distributed flow and pressure gradients. The versatile planar design facilitates custom fabricated channels with dimensions tuned for specific power requirements. The expansion of a single silicon-machined microchannel was demonstrated up to 5 mm in width for a 5 cm long channel, with power output comparable to the 5-microchannel array, i.e. scaling linearly. The ability of vertical stacking was also evaluated. Two 1 mm wide microchannels, placed on top of each other and separated by Kapton® electrodes, produced twice the power of a single channel without increasing the total volume of the fuel cell device. Note however that the overall power output of these devices was only about 1 mW or less, still restricted by transport and solubility of dissolved oxygen, and the fuel utilization was poor.

In contrast to film-deposited electrodes, the geometry and mechanical properties of rod-shaped electrodes enable unique three-dimensional microfluidic fuel cell architectures. An array architecture fuel cell was developed by Kjeang et al. [28] based on a hexagonal array of graphite rods mounted in a single cavity, as shown in Fig. 9. The array cell consisted of 29 graphite rods of 0.5 mm diameter with an average spacing of 0.2 mm, and the flow area in between the rods exhibited microfluidic flow characteristics similar to those of a planar unit cell. The cell had 12 anodes and 12 cathodes; 5 rods in the center were electrically insulated to compensate for the co-laminar inter-diffusion zone. When operated on the all-vanadium redox system, the array cell produced an order of magnitude more power than a planar unit cell without increasing

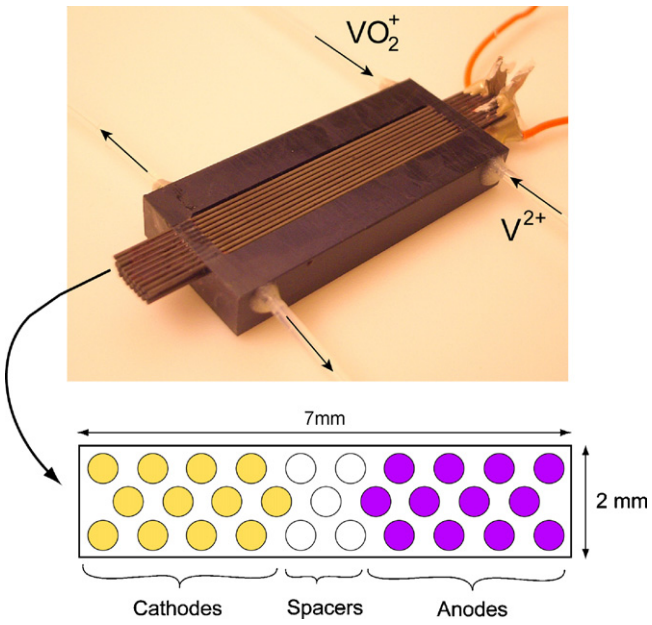

Fig. 9. Image and schematic of a microfluidic fuel cell expanded in three dimensions via the array cell architecture. Graphite rods are mounted in a single CNC-machined cavity. The cell comprises 12 anodes and 12 cathodes that are essentially independent. The five rods in the center of the device are exposed to co-laminar inter-diffusion of anolyte and catholyte and are not electrically connected. This architecture provides scalability in both vertical and horizontal directions. Reproduced with permission from Kjeang et al. [28]. Copyright Elsevier (2007).

the flow rate. Power and current levels of 28 mW and 86 mA were demonstrated, and the fuel utilization was significantly higher than that for the planar unit cell at any given flow rate. The array cell configuration may be readily expanded in both vertical (preferable) and horizontal directions to increase capacity. Scale-up requires only an enlarged cavity, in contrast to the volumetric costs of additional substrates and fluid handling networks associated with stacking of planar cells. However, the overall energy density of the array fuel cell system demonstrated here would ultimately be limited by the solubility and concentration of the vanadium redox species.

INI Power Systems have reported a prototype microfluidic fuel cell system based on the direct methanol laminar flow fuel cell technology [56]. The fuel cell system had been scaled up from a single channel to multiple channels in a planar array, while vertical scaling enabled a stacked design. A fuel and electrolyte separation and recirculation system was proposed that improved fuel efficiency at the cost of added complexity and reduced energy density of the complete fuel cell system. The performance levels and physical dimensions of the system were not provided.

5. Challenges and opportunities

Overall, the development of co-laminar microfluidic fuel cells to date has been tremendous, given that it is a relatively new invention. Research so far has resulted in operational devices with promising room-temperature performance in terms of power density and operational cell voltage. More must be done, however, to realize practical, efficient and competitive devices with high energy density and high fuel utilization. The most prominent constraint identified for current microfluidic fuel cells is their low energy density, defined as energy output per system volume or mass. The core physics of the co-laminar flow configuration require that both streams are liquid and contain an electrolyte. Although reactants may be added to the system at high concentration, the energy density of all devices presented hitherto has been low compared to other microstructured fuel cells due to the impractical single-pass use of liquid electrolyte without any form of recirculation or recycling. The implementation of a recirculation system for the electrolyte is a challenging task due to the space constraints and inevitable mixing/contamination issues. While fuel utilization data up to 100% per single pass have been presented, the fuel utilization at practical flow rates and useful cell voltages has generally been below 10%. In addition, there is a lack of engineering solutions for important functions such as integration of fuel and oxidant storage, waste handling, and low-power microfluidics-based fluid delivery (normally driven by a syringe pump via external tubing) using integrated micropumps and microvalves. With integrated infrastructure, microfluidic fuel cell units could be integrated on-chip as independent power sources for various MEMS-devices and microfluidic systems, as stand-alone units or in hybrid configurations in combination with small secondary batteries.

In contrast to the established mass transport limitation of dissolved oxygen-based cells, the performance of recent microfluidic fuel cell technology was typically restricted by a combination of mass transport, electrochemical kinetics, and ohmic resistance. All of these factors are discussed below.

Mass transport

Reactant transport from the bulk to the active sites primarily takes place by convection/diffusion, which can be enhanced by increasing the reactant concentrations and mean flow velocity or reducing the average cross-stream distance that a reactant molecule has to travel to reach the active site; or by choosing reactant species with higher diffusivity.

Electrochemical kinetics

Electrochemical limitations at the fuel cell electrodes are caused by activation overpotentials and slow reaction rates. Choosing appropriate electrocatalysts and increasing the overall active surface area of the electrodes are key methods to reduce these limitations. The choice of electrolyte media and pH may also influence the electrochemical kinetics. Furthermore, the kinetics would benefit from raising the operational temperature, which is normally not practical for microfluidic fuel cells. A heat exchange or recirculation system of 'used' electrolyte heated up by the cell reaction may however provide an avenue towards increased operational temperature.

Ohmic resistance

The combined ohmic resistance of a microfluidic fuel cell includes ionic charge transfer resistance in the electrolyte and electrical resistance in electrodes, contacts, and wires; all of which need to be minimized for an efficient fuel cell system. Overall ohmic losses are directly proportional to the cell current, and as demonstrated by the fuel cells with flow-through porous electrode architecture [43,44], the detrimental effects of ohmic resistance become increasingly important for devices with high power density. The solution resistance can be reduced by employing a strong supporting electrolyte with high concentration and minimizing the average charge transfer distance between the electrodes. Particularly in the case of the flow-through porous electrode architecture [43,44], an additional highly conductive third stream introduced between the electrodes may be advantageous, albeit at the cost of increased complexity. Electrical resistance may be reduced further by incorporating highly conductive current collectors.

The development of microfluidic fuel cell technology would largely benefit from further theoretical and numerical modeling

of these performance-limiting factors, as well as system modeling and optimization of established cell architectures. Only a handful of modeling contributions have been reported to date. For example, no modeling efforts have yet been applied to the air-breathing microfluidic fuel cell architecture or any of the microfluidic vanadium redox fuel cells. Exploration of key mechanisms would be useful, including the charge transfer mechanism in the flowing electrolyte and the species transport mechanism for flow inside a porous electrode. Various experimental diagnostic techniques such as electrochemical impedance spectroscopy could be implemented to analyze these mechanisms and to verify new theoretical and modeling approaches.

A wide variety of single planar microfluidic fuel cell technologies have been demonstrated so far. Most of these fuel cells were un-optimized proof-of-concept devices with wide-ranging opportunities for further improvements. New fuel and oxidant combinations are still possible, and the prospects of finding new electrolytes with advanced functionality are high, for example ionic liquids and non-aqueous solvents, as well as novel techniques for phase separation at the co-laminar interface enabled by the use of immiscible solvents, density and viscosity gradients, or magnetic fields. The opportunities for two-phase flows are numerous, with the fuel carried in one phase and the oxidant in the other. In addition, novel cell architectures that accommodate gaseous components would conceivably have a large impact. There is also ample opportunity to improve the micro- and nano-structure of the electrodes employed in microfluidic fuel cells; an ideal electrode would incorporate a wide range of characteristic length scales from nanometres to millimetres and have a very large active surface area associated with a porous solid–liquid interface. The enhanced surface to volume ratio attributed to miniaturization can also be further exploited by reducing the characteristic size of the microchannels while keeping the parasitic pumping power requirements below a practical threshold.

To enable wide-spread commercialization, the cost of a microfluidic fuel cell system must also be considered. Microfluidic fuel cell technology has high potential for cost-effective units attributed to inexpensive fabrication techniques and the elimination of the membrane and its associated issues. Strategic cost reductions on the unit cell level are possible in several areas, including materials, manufacturing procedures, and the choice (and source) of fuel, oxidant and electrolyte. Given the high cost of precious metal catalysts, advanced catalyst supports with low catalyst loading and high surface area are highly desired, as is the implementation of low-cost alternative catalysts. Furthermore, the cost associated with fueling infrastructure would be avoided by a fuel/oxidant regeneration scheme.

The power output of a single planar microfluidic fuel cell is inadequate for most practical applications. The feasibility of enlarging a planar unit cell, i.e. increasing the geometrical area of electrodes and microchannel, is limited by structural constraints, increased crossover, and increased ohmic losses if the average distance between anodic and cathodic active sites becomes large. In order to produce adequate power, multiple independent unit cells could be accommodated in a single plane, and then these planes could be stacked as in typical PEM fuel cells. The volumetric power density of such devices would however be limited by the volume of the sealing and structural elements separating the cells. In traditional PEM fuel cell stacks, which are limited by similar issues [78], the bi-polar plates serve as structural and electrical components. The inherent advantage of non-planar electrode–electrolyte interfaces has been recognized and demonstrated for such cells using, for example, waved membrane-electrode assemblies [78]. In contrast, the microfluidic fuel cells presented to date contain mostly non-participating structural materials such as glass or PDMS. The scale-up of microfluidic fuel cell technology in a volumetrically efficient manner remains a challenge. The expansion methodologies reported so far have confirmed that microfluidic fuel cell technology and the associated manufacturing processes are well-suited for scale-up, but the volumetric energy density of the prototype devices was insufficient for actual applications and the total power output was less than 0.1 W. The realization of a scalable microfluidic fuel cell system that combines a competitive energy density with a useful power output in the range of 1–20 W will be a very challenging task that requires significant innovation and optimization on both unit cell and stack levels.

Microfluidic fuel cell architectures are well-suited for integration with biofuel cell technology and can aid in the development of practical biofuel cell devices. The development of biofuel cells has typically focused on individual enzyme electrodes and immobilization schemes while little progress has been made in terms of system-level engineering [8]. The performance of the biofuel cells presented so far was inadequate for practical applications, mainly due to the low power density and low stability. Yet, the current densities of biocatalytic electrodes using enzymes immobilized in redox hydrogels were frequently controlled by the diffusive transport of reactant from the bulk solution to the active polymer matrix, for both glucose bioanodes [79,80] and oxygen biocathodes [81–83]. Moreover, biocathodes based on bilirubin oxidase or laccase enzymes have outperformed platinum in terms of reduced overpotential and enhanced activity towards oxygen reduction [81–83]. Biofuel cells stand to benefit from development of microfluidic fuel cell technologies through (i) enhancing convective mass transport, enabling higher enzyme loading while maintaining the enzymatic turnover rates close to their full capability, (ii) harnessing the high surface to volume ratio inherent to microstructured devices to promote the surface-based electrochemical reactions catalyzed by the immobilized enzymes, and (iii) providing useful scale-up opportunities for practical devices with automated reactant supply and on-chip integration compatible with MEMS-technologies. As suggested by Bullen et al. [8], future efforts should also target low-cost genetically engineered biocatalytic enzymes with high turnover rate, and most importantly, improved stability and lifetime of enzymatic electrodes. Microfluidic devices with automated reactant supply are well-suited for stability analyses as they provide steady state operation under fixed conditions while keeping each enzyme in an optimum environment.

6. Conclusions

The research efforts in the area of microfluidic fuel cell technology have increased substantially to date, considering the relatively recent invention in 2002. As of 2007, the field holds over 30 scientific publications. Functional devices have been introduced based on various fuels and oxidants, with competitive power densities and cell voltages obtained at room temperature. The levels of fuel utilization have been raised from below 1% to nearly 100% per single pass, and several scale-up methodologies have been demonstrated. To facilitate a major commercial break-through, however, much further work is required. The main challenge is to develop a microfluidic fuel cell system, including auxiliary equipment and fluid storage, with high overall energy density and power output in the 1–20 W range. The research opportunities in this field are numerous, ranging from unit cell level improvements via expansion and scale-up methodologies to system integration including fueling infrastructure and waste handling. Finally, microfluidic fuel cell technology is vital for the development of practical biofuel cells, and a swell of research interest in this area is anticipated.

Acknowledgments

This research was funded by the Natural Sciences and Engineering Research Council of Canada (NSERC) and Angstrom Power Inc. Infrastructure funding from Canada Foundation for Innovation (CFI) and the British Columbia Knowledge Development Fund (BCKDF) is highly appreciated.

References

[1] J. Larminie, A. Dicks, Fuel Cell Systems Explained, John Wiley & Sons Inc., Hoboken, NJ, 2003.
[2] C.K. Dyer, Journal of Power Sources 106 (2002) 31–34.
[3] A. Kundu, J.H. Jang, J.H. Gil, C.R. Jung, H.R. Lee, S.H. Kim, B. Ku, Y.S. Oh, Journal of Power Sources 170 (2007) 67–78.
[4] J.D. Morse, International Journal of Energy Research 31 (2007) 576–602.
[5] N.T. Nguyen, S.H. Chan, Journal of Micromechanics and Microengineering 16 (2006) R1–R12.
[6] W.M. Qian, D.P. Wilkinson, J. Shen, H.J. Wang, J.J. Zhang, Journal of Power Sources 154 (2006) 202–213.
[7] A.K. Shukla, R.K. Raman, K. Scott, Fuel Cells 5 (2005) 436–447.
[8] R.A. Bullen, T.C. Arnot, J.B. Lakeman, F.C. Walsh, Biosensors & Bioelectronics 21 (2006) 2015–2045.
[9] E. Katz, A.N. Shipway, I. Willner, Biochemical Fuel Cells, in: W. Vielstich, H.A. Gasteiger, A. Lamm (Eds.), Handbook of Fuel Cells—Fundamentals, Technology and Applications, vol. 1, John Wiley & Sons, Ltd., New York, 2003.
[10] B.E. Logan, B. Hamelers, R. Rozendal, U. Schrorder, J. Keller, S. Freguia, P. Aelterman, W. Verstraete, K. Rabaey, Environmental Science & Technology 40 (2006) 5181–5192.
[11] B.E. Logan, J.M. Regan, Environmental Science & Technology 40 (2006) 5172–5180.
[12] J. Kim, H.F. Jia, P. Wang, Biotechnology Advances 24 (2006) 296–308.
[13] S.C. Barton, J. Gallaway, P. Atanassov, Chemical Reviews 104 (2004)4867–4886.
[14] S. Pennathur, J.C.T. Eijkel, A. van den Berg, Lab on a Chip 7 (2007) 1234–1237.
[15] G.M. Whitesides, Nature 442 (2006) 368–373.
[16] N.T. Nguyen, S.T. Wereley, Fundamentals and Applications of Microfluidics, Artech House, Boston, MA, 2002.
[17] T.M. Squires, S.R. Quake, Reviews of Modern Physics 77 (2005) 977–1026.
[18] M. Gad-el-Hak, Physics of Fluids 17 (2005).
[19] D. Erickson, Microfluidics and Nanofluidics 1 (2005) 301–318.
[20] C.T. Crowe, D.F. Elger, J.A. Roberson, Engineering Fluid Mechanics, John Wiley & Sons Inc., New York, 2001.
[21] J. Atencia, D.J. Beebe, Nature 437 (2005) 648–655.
[22] R.F. Ismagilov, A.D. Stroock, P.J.A. Kenis, G. Whitesides, H.A. Stone, Applied Physics Letters 76 (2000) 2376–2378.
[23] S.K. Yoon, M. Mitchell, E.R. Choban, P.J.A. Kenis, Lab on a Chip 5 (2005) 1259–1263.
[24] A.E. Kamholz, B.H. Weigl, B.A. Finlayson, P. Yager, Analytical Chemistry 71 (1999) 5340–5347.
[25] J.B. Salmon, C. Dubrocq, P. Tabeling, S. Charier, D. Alcor, L. Jullien, F. Ferrage, Analytical Chemistry 77 (2005) 3417–3424.
[26] J.P. Brody, P. Yager, Sensors and Actuators A: Physical 58 (1997) 13–18.
[27] P.J.A. Kenis, R.F. Ismagilov, G.M. Whitesides, Science 285 (1999) 83–85.
[28] E. Kjeang, J. McKechnie, D. Sinton, N. Djilali, Journal of Power Sources 168 (2007) 379–390.
[29] J.C. McDonald, D.C. Duffy, J.R. Anderson, D.T. Chiu, H.K. Wu, O.J.A. Schueller, G.M. Whitesides, Electrophoresis 21 (2000) 27–40.
[30] Y.N. Xia, G.M. Whitesides, Annual Review of Materials Science 28 (1998) 153–184.
[31] D.C. Duffy, J.C. McDonald, O.J.A. Schueller, G.M. Whitesides, Analytical Chemistry 70 (1998) 4974–4984.
[32] E. Kjeang, A.G. Brolo, D.A. Harrington, N. Djilali, D. Sinton, Journal of the Electrochemical Society 154 (2007) B1220–B1226.
[33] J.N. Lee, C. Park, G.M. Whitesides, Analytical Chemistry 75 (2003)6544–6554.
[34] R. Ferrigno, A.D. Stroock, T.D. Clark, M. Mayer, G.M. Whitesides, Journal of the American Chemical Society 124 (2002) 12930–12931.
[35] W. Sung, J.-W. Choi, Journal of Power Sources 172 (2007) 198–208.
[36] E.R. Choban, J.S. Spendelow, L. Gancs, A. Wieckowski, P.J.A. Kenis, Electrochimica Acta 50 (2005) 5390–5398.
[37] E.R. Choban, P. Waszczuk, P.J.A. Kenis, Electrochemical and Solid State Letters 8 (2005) A348–A352.
[38] R.S. Jayashree, D. Egas, J.S. Spendelow, D. Natarajan, L.J. Markoski, P.J.A. Kenis, Electrochemical and Solid State Letters 9 (2006) A252–A256.
[39] R.S. Jayashree, L. Gancs, E.R. Choban, A. Primak, D. Natarajan, L.J. Markoski, P.J.A. Kenis, Journal of the American Chemical Society 127 (2005) 16758–16759.
[40] A. Li, S.H. Chan, N.T. Nguyen, Journal of Micromechanics and Microengineering 17 (2007) 1107–1113.
[41] J.L. Cohen, D.J. Volpe, D.A. Westly, A. Pechenik, H.D. Abruna, Langmuir 21 (2005) 3544–3550.
[42] J.L. Cohen, D.A. Westly, A. Pechenik, H.D. Abruna, Journal of Power Sources 139 (2005) 96–105.
[43] E. Kjeang, R. Michel, D. Sinton, N. Djilali, D.A. Harrington, Electrochimica Acta 54 (2008) 698–705.
[44] E. Kjeang, R. Michel, D.A. Harrington, N. Djilali, D. Sinton, Journal of the American Chemical Society 130 (2008) 4000–4006.
[45] E. Kjeang, B.T. Proctor, A.G. Brolo, D.A. Harrington, N. Djilali, D. Sinton, Electrochimica Acta 52 (2007) 4942–4946.
[46] E.R. Choban, L.J. Markoski, A. Wieckowski, P.J.A. Kenis, Journal of Power Sources 128 (2004) 54–60.
[47] S.M. Mitrovski, L.C.C. Elliott, R.G. Nuzzo, Langmuir 20 (2004) 6974–6976.
[48] S.M. Mitrovski, R.G. Nuzzo, Lab on a Chip 6 (2006) 353–361.
[49] M. Togo, A. Takamura, T. Asai, H. Kaji, M. Nishizawa, Electrochimica Acta 52 (2007) 4669–4674.
[50] S. Hasegawa, K. Shimotani, K. Kishi, H. Watanabe, Electrochemical and Solid State Letters 8 (2005) A119–A121.
[51] C.M. Moore, S.D. Minteer, R.S. Martin, Lab on a Chip 5 (2005) 218–225.
[52] M.H. Sun, G.V. Casquillas, S.S. Guo, J. Shi, H. Ji, Q. Ouyang, Y. Chen, Microelectronic Engineering 84 (2007) 1182–1185.
[53] K.S. Salloum, J.R. Hayes, C.A. Friesen, J.D. Posner, Journal of Power Sources 180 (2008) 243–252.
[54] M. Togo, A. Takamura, T. Asai, H. Kaji, M. Nishizawa, Journal of Power Sources 178 (2008) 53–58.
[55] T.C. Merkel, V.I. Bondar, K. Nagai, B.D. Freeman, I. Pinnau, Journal of Polymer Science Part B: Polymer Physics 38 (2000) 415–434.
[56] L.J. Markoski, The laminar flow fuel cell: a portable power solution, in: 8th Annual International Symposium Small Fuel Cells 2006, Small Fuel Cells for Portable Applications, The Knowledge Foundation, Washington, DC, 2006.
[57] C.P. de Leon, F.C. Walsh, A. Rose, J.B. Lakeman, D.J. Browning, R.W. Reeve, Journal of Power Sources 164 (2007) 441–448.
[58] G.H. Miley, N. Luo, J. Mather, R. Burton, G. Hawkins, L.F. Gu, E. Byrd, R. Gimlin, P.J. Shrestha, G. Benavides, J. Laystrom, D. Carroll, Journal of Power Sources 165 (2007) 509–516.
[59] N.A. Choudhury, R.K. Raman, S. Sampath, A.K. Shukla, Journal of Power Sources 143 (2005) 1–8.
[60] R. Aogaki, E. Ito, M. Ogata, Journal of Solid State Electrochemistry 11 (2007) 757–762.
[61] L. Gu, N. Luo, G.H. Miley, Journal of Power Sources 173 (2007) 77–85.
[62] C.P. de Leon, A. Frias-Ferrer, J. Gonzalez-Garcia, D.A. Szanto, F.C. Walsh, Journal of Power Sources 160 (2006) 716–732.
[63] W. SkyllasKazacos, C. Menictas, M. Kazacos, Journal of the Electrochemical Society 143 (1996) L86–L88.
[64] A. Bazylak, D. Sinton, N. Djilali, Journal of Power Sources 143 (2005) 57–66.
[65] M.H. Chang, F. Chen, N.S. Fang, Journal of Power Sources 159 (2006) 810–816.
[66] F.L. Chen, M.H. Chang, M.K. Lin, Electrochimica Acta 52 (2007) 2506–2514.
[67] W.Y. Chen, F.L. Chen, Journal of Power Sources 162 (2006) 1137–1146.
[68] F. Chen, M.-H. Chang, C.-W. Hsu, Electrochimica Acta 52 (2007) 7270–7277.
[69] S.K. Yoon, G.W. Fichtl, P.J.A. Kenis, Lab on a Chip 6 (2006) 1516–1524.
[70] A.D. Stroock, S.K.W. Derringer, A. Ajdari, I. MeziÃ, H.A. Stone, G.M. Whitesides, Science 295 (2002) 647.
[71] J.D. Kirtland, G.J. McGraw, A.D. Stroock, Physics of Fluids 18 (2006).
[72] K.G. Lim, G.T.R. Palmore, Biosensors & Bioelectronics 22 (2007) 941–947.
[73] J. Lee, K.G. Lim, G.T.R. Palmore, A. Tripathi, Analytical Chemistry 79 (2007) 7301–7307.
[74] I. Willner, E. Katz, Angewandte Chemie-International Edition 39 (2000) 1180–1218.
[75] N.L. Akers, C.M. Moore, S.D. Minteer, Electrochimica Acta 50 (2005) 2521–2525.
[76] S. Topcagic, S.D. Minteer, Electrochimica Acta 51 (2006) 2168–2172.
[77] E. Kjeang, D. Sinton, D.A. Harrington, Journal of Power Sources 158 (2006) 1–12.
[78] W.R. Merida, G. McLean, N. Djilali, Journal of Power Sources 102 (2001) 178–185.
[79] N. Mano, F. Mao, A. Heller, Journal of Electroanalytical Chemistry 574 (2005) 347–357.
[80] N. Mano, F. Mao, A. Heller, Chembiochem 5 (2004) 1703–1705.
[81] N. Mano, J.L. Fernandez, Y. Kim, W. Shin, A.J. Bard, A. Heller, Journal of the American Chemical Society 125 (2003) 15290–15291.
[82] V. Soukharev, N. Mano, A. Heller, Journal of the American Chemical Society 126 (2004) 8368–8369.
[83] N. Mano, V. Soukharev, A. Heller, Journal of Physical Chemistry B 110 (2006) 11180–11187.